Controls on sinking velocities and mass fluxes of size-fractionated marine particles in recent U.S. GEOTRACES cruises

Yang Xiang[1], Phoebe J. Lam[2], and Adrian B. Burd[3]

[1]Department of Ocean Sciences, University of California at Santa Cruz
[2]University of California, Santa Cruz
[3]University of Georgia

November 23, 2022

Abstract

Particle composition is an important parameter that influences sinking velocity of marine particles. Most current studies, however, are limited by either a lack of routine measurements of particle composition or low sampling resolution in the water column. Here, we compile full ocean-depth size-fractionated (1-51 and >51 μm) particle concentration and composition of suspended particulate matter from three recent U.S. GEOTRACES cruises to calculate their corresponding sinking velocity and mass flux. Our model is based on Stokes' Law and incorporates a newly updated power-law relationship between particle size and porosity. The integration of the porosity-size relationship decreases the power applied to size in Stokes' Law to 0.8. The medians of average sinking velocity in total particles are 15.4, 15.2, and 7.4 m/d, in the North Atlantic, Southeast Pacific, and western Arctic Ocean, respectively. We examine the relative importance of particle concentration, composition, size, and hydrography on sinking fluxes. Particle concentration is the major control of the variability and magnitude of mass flux, while particle composition is the second most important term. Increasing porosity with aggregate size and a dominance of smaller particles diminishes the importance of the size dependence in mass flux, elevating the relative importance of composition and thus density. Viscosity of seawater can result in up to a factor of two difference in mass flux between polar and tropical oceans. This work serves as one of the first studies to offer quantitative perspectives for the contribution from different factors to mass flux in field observations of marine particles.

Controls on sinking velocities and mass fluxes of size-fractionated marine particles in recent U.S. GEOTRACES cruises

Yang Xiang[1,*], Phoebe J. Lam[1], Adrian B. Burd[2]

[1]Department of Ocean Sciences, University of California, Santa Cruz, CA 95064 USA
[2]Department of Marine Sciences, University of Georgia, Athens, GA 30602 USA

*Corresponding author: Yang Xiang, E: yaxiang@ucsc.edu, P: 1-831-212-5119
University of California Santa Cruz, 1156 High Street, Santa Cruz, CA 95064

Key Points:

- Incorporation of ballast minerals into natural marine aggregates away from the sediment resuspension is likely not to alter particle size;
- The effect of size on total mass flux is often not as important as particle composition, due to particle mass partitioning and porosity;
- The western Arctic Ocean is characterized by lowest total mass flux due to its small sizes, low particle concentrations and viscous water.

Abstract

Particle composition is an important parameter that influences sinking velocity of marine particles. Most current studies, however, are limited by either a lack of routine measurements of particle composition or low sampling resolution in the water column. Here, we compile full ocean-depth size-fractionated (1-51 and >51 μm) particle concentration and composition of suspended particulate matter from three recent U.S. GEOTRACES cruises to calculate their corresponding sinking velocity and mass flux. Our model is based on Stokes' Law and incorporates a newly updated power-law relationship between particle size and porosity. The integration of the porosity-size relationship decreases the power applied to size in Stokes' Law to 0.8. The medians of average sinking velocity in total particles are 15.4, 15.2, and 7.4 m/d, in the North Atlantic, Southeast Pacific, and western Arctic Ocean, respectively. We examine the relative importance of particle concentration, composition, size, and hydrography on sinking fluxes. Particle concentration is the major control of the variability and magnitude of mass flux, while particle composition is the second most important term. Increasing porosity with aggregate size and a dominance of smaller particles diminishes the importance of the size dependence in mass flux, elevating the relative importance of composition and thus density. Viscosity of seawater can result in up to a factor of two difference in mass flux between polar and tropical oceans. This work serves as one of the first studies to offer quantitative perspectives for the contribution from different factors to mass flux in field observations of marine particles.

Plain language summary

In this study, we compile concentrations and chemical compositions of marine suspended particles from the surface to seafloor on a global scale, and evaluate potential factors controlling the particle sinking flux. Estimating how fast particles sink and the magnitude of particle flux can help us better understand the global carbon budget. Our results demonstrate the primary importance of particle concentration affecting the particle flux. For example, at places with higher biological production and thereby higher particle concentrations, samples collected are characterized by increased particle flux. Other factors, such as the chemical composition and size of marine particles and viscosity of seawater compete for influence: some mineral phases in particles, characterized by higher densities, potentially offer excess weights to enhance the particle flux; smaller particles tend to sink slower compared to larger particles because of their sizes. In the high-latitude Arctic Ocean, marine particles have high concentrations of ballasting minerals, however, this alone cannot outcompete the most viscous water, smallest particle size and concentrations, leading to much smaller mass fluxes compared to tropical oceans.

Keywords: Sinking velocity, Total mass flux, Porosity, Ballast effect, Biological pump, GEOTRACES

1. Introduction

The marine biological carbon pump (BCP) plays a crucial role in the global carbon cycle by fixing carbon dioxide (CO_2) in the surface water into particulate organic matter (POM), which then sinks into the deep ocean (Kwon et al., 2009; Volk & Hoffert, 1985). Particle dynamics in the water column, including particle remineralization, aggregation, and disaggregation, are of significance in modifying and attenuating POM during sinking (Lam & Marchal, 2015). Most of the sinking flux is composed of phytodetrital aggregates, marine snow, and fecal pellets (Alldredge & Silver, 1988; Bishop et al., 1977; Ebersbach & Trull, 2008; Fowler & Knauer, 1986; Laurenceau-Cornec et al., 2015a; Turner, 2015; Wilson et al., 2013). Only a small fraction of POM (~10%) produced at the surface, however, sinks below mesopelagic regions (Martin et al., 1987).

Conceptually, vertical mass flux is calculated as the product of the sinking velocity and particle concentration. It is closely related to particle properties, such as concentration, size, and composition. While particle flux should scale with concentration, this is modulated by variations in sinking speed caused by differences in particle size, shape, and excess density. Numerous studies measure POC fluxes using sediment traps (e.g., Buesseler et al., 2007), and POC concentrations using large-volume filtration (e.g., Bishop et al., 1977; Lam et al., 2011). Variations in the relationship between flux and concentration reflect the variation in sinking speed. The importance of particle size on carbon export is apparent from Stokes' Law (Stokes, 1851), which shows that the sinking velocity is proportional to the square of particle diameter. Despite only holding for spherical solid particles at low Reynolds number, Stokes' Law has been widely used to characterize the sinking speed of marine particles (e.g., Laurenceau-Cornec et al., 2020; McDonnell & Buesseler, 2010; Omand et al., 2020), giving insights into the complicated system of the BCP. Similar to particle size, particle composition is also known to affect the export flux via its relationship with sinking velocity. The existence of mineral ballast, such as $CaCO_3$ and lithogenic particles, has been suggested to provide a source of excess density and/or protection and promote carbon export into the deep ocean (Armstrong et al., 2001; Francois et al., 2002; Klaas & Archer, 2002). Opal is a less efficient ballast mineral as a result of its lower density and/or higher porosity (Bach et al., 2016; Francois et al., 2002; Iversen & Ploug, 2010; Lam & Bishop, 2007; Lam et al., 2011; Puigcorbé et al., 2015). The ballast effect, however, is still under active debate (Aumont et al., 2017; Boyd & Trull, 2007; Henson et al., 2012; Lam & Bishop, 2007; Le Moigne et al., 2012; Lee et al., 2009; Rosengard et al., 2015), since indirect ecosystem effects are difficult to disentangle from direct effects of mineral density (e.g., Lima et al., 2014).

Thanks to the GEOTRACES program, measurements of particle concentration and composition in the North Atlantic, equatorial Southeast Pacific, and western Arctic Ocean have been made in the past decade, covering many different geographic regions (Lam et al., 2018; Lam et al., 2015; Xiang & Lam, 2020). The three ocean basins are characterized by different sources of particles, therefore different particle compositions. This study utilizes the composition data from these recent U.S. GEOTRACES cruises and applies mass-size and porosity-size power-law functions to calculate the corresponding size-fractionated sinking velocity and mass flux. Despite lacking the seasonal resolution, this data offers higher spatial and depth resolution of sinking particle fluxes than existing sediment traps, and allows us to investigate the relative importance of particle concentration, composition (density), particle size, and hydrography on particle sinking fluxes. Indeed, the model used here can be adapted to any other size-fractionated particulate phases and trace metals to calculate their corresponding mass fluxes, given the assumption that the specific particulate phase has the same sinking rate as the bulk particles. Insights gained in this study help us understand the role of particle characteristics on carbon flux, which can be applied

to other regions in future studies to improve our understanding of the biological pump on a global scale. It is particularly important, for most model projections suggest a decline in the carbon export to the deep ocean under the current warming scenario (Bopp et al., 2013; Cavan et al., 2019; Laufkötter et al., 2016).

2. Materials and Methods

2.1 Cruise tracks and sampling method

The U.S. GEOTRACES North Atlantic Zonal Transect (GA03) cruise, was completed with two legs in 2010-2011 in the subtropical North Atlantic (Figure 1). The cruise track sampled the Mauritanian Upwelling system, the North Atlantic deep western boundary current, and the Trans-Atlantic Geotraverse (TAG) hydrothermal plume on the slowly-spreading Mid-Atlantic Ridge. The Eastern Pacific Zonal Transect (GP16) cruise was completed in the Southeast (SE) Pacific Ocean in October–December 2013 (Figure 1). The expedition sampled the Peruvian Coastal upwelling region, the oxygen deficient zone (ODZ) off Peru, and the superfast-spreading East Pacific Rise (EPR) hydrothermal plume. The U.S. Arctic cruise (GN01) focused on the western Arctic Ocean and sampled at both very productive shallow shelves and extremely oligotrophic deep basins in 2015 (Figure 1). The Arctic Ocean is characterized by extremely broad continental shelves, consisting of 53% of its overall area (Jakobsson, 2002).

Size-fractionated particles were all sampled using dual-flow McLane Research in-situ pumps (WTS-LV). Large size fraction particles are referred to as "LSF", representing the size fraction of >51 μm, whereas the small size fraction, "SSF", are particles between 1 and 51 μm. Total particles are defined as the sum of both size fractions (Total= LSF+SSF). More details about the cruise hydrography, sample handling and analytical methods of different particle compositions can be found in Lam et al. (2015), Lam et al. (2018), Xiang and Lam (2020).

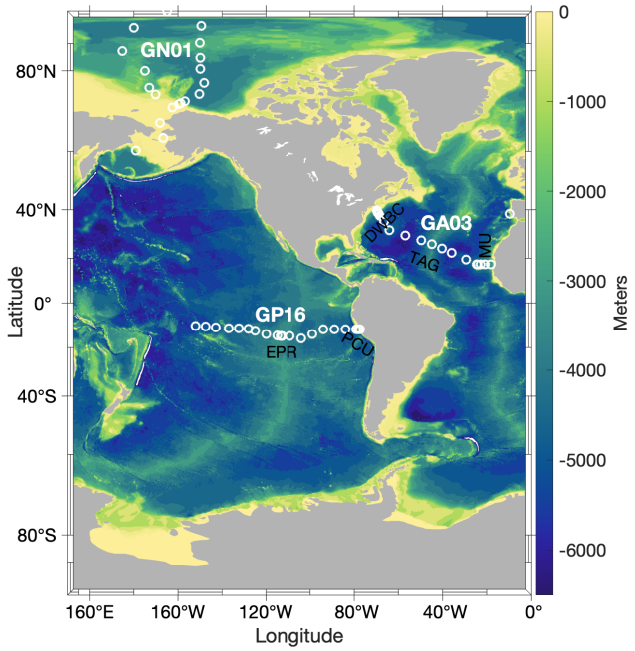

Figure 1. Station map of three U.S. GEOTRACES cruises in which in-situ pump were deployed. The color bar is ocean bathymetry (using *haline* in cmocean colormap) (Thyng et al., 2016). The GA03 is the North Atlantic Zonal Transect, GP16 is the Eastern Pacific Zonal Transect, and GN01

is the Arctic cruise. MU: Mauritanian Upwelling; TAG: Trans-Atlantic Geotraverse hydrothermal plume; DWBC: deep western boundary current; PCU: Peruvian Coastal Upwelling; EPR: East Pacific Rise (EPR) hydrothermal plume.

2.2 Porosity and size relationship

The porosity is defined as the volume fraction of an aggregate that is not occupied by solid matter and tends to increase with particle size (Alldredge & Gotschalk, 1988). It is an essential parameter in the calculation of particle volume and mass flux from size (Jackson et al., 1997; Stemmann et al., 2008). Alldredge and Gotschalk (1988) pioneered porosity measurements in marine aggregates and found a power-law relationship between the porosity and particle size by direct measurements in situ:

$$1\text{-}P_i = (8\times10^{-3})\times(d_i/10^3)^{-1.6} \quad (1)$$

where P_i is the particle porosity for size bin i and is unitless, d_i is the equivalent spherical diameter of particles (μm), and 10^3 is the conversion factor between μm and mm. This classic power function was used to calculate the particle sinking velocities in many studies (e.g., Burd et al., 2007; Ruiz, 1997). Data points from Alldredge and Gotschalk (1988) were extracted using WebPlotDigitizer (Rohatgi, 2010) for this study. The extracted regression equation is $1\text{-}P_i = (8.2\times10^{-3})\times(d_i/10^3)^{-1.6}$, which is similar to the original one.

In the past 30 years, there have been several additional studies measuring porosity and size of marine aggregates (Figure 2) (Bach et al., 2016; Engel et al., 2009; Iversen & Robert, 2015; Lam & Bishop, 2007; Laurenceau-Cornec et al., 2020; Laurenceau-Cornec et al., 2015b; Logan & Alldredge, 1989; Ploug et al., 2008a; Ploug & Passow, 2007; Prairie et al., 2015; Schmidt et al., 2014). A detailed summary of all data sources and analytical methods is listed in Table S1. Due to the difficulties of measuring size and porosity in situ in the water column, many of these studies were conducted with aggregates formed in lab roller tanks, while others measured bulk properties from which we estimated particle size distributions. For example, the Lam and Bishop (2007) study estimated porosities of bulk size-fractionated (1-51 μm and >51 μm) particles collected by in-situ filtration in the Southern Ocean. To estimate a mean particle size for each size fraction to associate with estimated porosities, we used nearby particle size distributions obtained by the Underwater Vision Profiler (UVP) in the Lohafex 2009 and Tara 2011 cruises in the Subantarctic and Antarctic, respectively (Picheral et al., 2017). It is noted that natural aggregates are different from aggregates formed in roller tanks and characterized by smaller sizes (Laurenceau-Cornec et al., 2015b). Further, for a given size, it also seems that natural aggregates have a higher porosity (lower $(1\text{-}P_i)$) than similarly-sized lab formed aggregates (Figure 2). Since marine particles are all collected in situ in our dataset, we only use natural marine particles in our updated regression.

Compared to Eq. 1, we also used a different linear regression model. The ordinary least square (OLS) regression used in Alldredge and Gotschalk (1988) is sensitive to changes in X-axis scale (i.e., meter vs. millimeter). Therefore, a Model-II reduced major axis (RMA) regression was used, as implemented in lsqfitgm.m in MATLAB by E.T. Peltzer (https://www.mbari.org/index-of-downloadable-files/). The updated power-law relationship between (1-porosity) and particle sizes is:

$$1\text{-}P_i = (3.6\times10^{-3})\times(d_i/10^3)^{-1.2} \quad (2)$$

Compared to the original Alldredge and Gotschalk (1988) relationship (Eq. 1), this new relationship has a weaker dependency of porosity with size, but also has a lower coefficient. Logan and Wilkinson (1990) illustrated the relationship between the fractal dimension D_3 and the power

exponent b in the porosity-size function, where D_3=3+b. The value of the fractal dimension depicts how much space the solid occupies in three dimensions. A pure solid has a fractal dimension of 3. The fractal dimensions in our updated and original Alldredge and Gotschalk (1988) relationship are 1.8 and 1.4, respectively, which means that marine particles in this study are more compact than those in Alldredge and Gotschalk (1988). Despite the higher fractal dimension in our new relationship, the coefficient is lower, resulting in higher porosities over the size range of most marine particles (Figure 2). The intersection between the original Eq. 1 and new Eq. 2 occurs at 8.3 mm; therefore, particles smaller than 8.3 mm have a higher porosity (lower 1-P_i) in the newly compiled porosity-size relationship (Figure 2). Additionally, the new relationship predicts a particle size of about 8.6 μm when the porosity approaches 0, compared to 48.9 μm for the original Alldredge and Gotschalk (1988) relationship. We treat particles as pure solids (P_i=0) for all sizes below 8.6 μm.

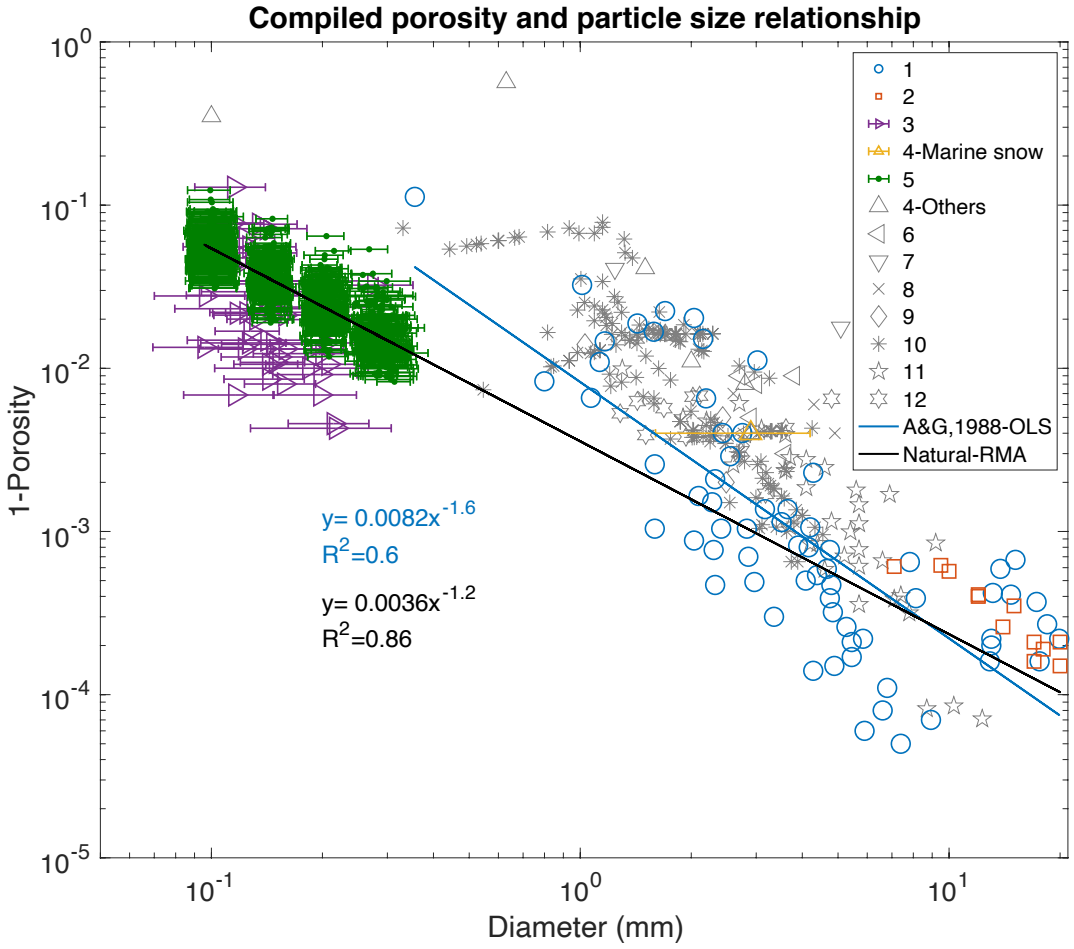

Figure 2. The newly compiled porosity-size relationship from literature. Data points outlined in gray are aggregates formed in lab roller tanks, whereas colored symbols are natural marine aggregates. The ordinary least square (OLS) and reduced major axis (RMA) regression are used to fit data from Alldredge and Gotschalk (1988) and all natural aggregates, respectively. Regression equations are displayed with the colors matching with fit lines. 1: Alldredge and Gotschalk (1988); 2: Logan and Alldredge (1989); 3: Lam and Bishop (2007); 4: Ploug et al. (2008a); 5: Bach et al. (2016); 6: Ploug and Passow (2007); 7: Engel et al. (2009); 8: Schmidt et

al. (2014); 9: Prairie et al. (2015); 10: Iversen and Robert (2015); 11: Laurenceau-Cornec et al. (2015b); 12: Laurenceau-Cornec et al. (2020).

2.3 Particle sinking rate calculation

Stokes' Law has been widely used to calculate sinking velocities of marine particles (Stokes, 1851). In this simple model assuming spherical particles, laminar flow, and a smooth surface, the sinking velocity increases with particle size and excess density, the density difference between solid materials and seawater:

$$W_i = \frac{g\Delta\varrho(d_i/10^6)^2}{18\eta} \quad (3)$$

where W_i is the sinking velocity for size bin i with the unit of m/s, g is the gravitational acceleration in m/s^2, $\Delta\varrho$ is the excess density in kg/m^3, 10^6 is the conversion factor between μm and m, and η is the dynamic viscosity of seawater in kg/m/s. Considering porosity, and assuming that flow through the porous aggregate is negligible (although see section 4.4), Eq. 3 becomes:

$$W_i = (1-P_i)\frac{g\Delta\varrho(d_i/10^6)^2}{18\eta} \quad (4)$$

Combing Eqs. 2 and 4 explicitly and using m as the unit for particle size, the sinking velocity is calculated as:

$$W_i = (3.6\times10^{-11.4})\times\frac{g\Delta\varrho(d_i)^{0.8}}{18\eta} \quad (5)$$

Since $1-P_i$ decreases (porosity increases) with particle size (Eqs. 1-2), sinking velocities in Eqs. 4-5 have a weaker dependence on the particle size compared to the original Stokes' Law (Eq. 3). As a result, the influence of other parameters, such as the excess density and viscosity, becomes more important. It is also worth noting that a slightly stronger size dependency in sinking velocity occurs with the implementation of the newly compiled porosity and size relationship (Eq. 2) to Eq. 5 when compared to using the original relationship from Alldredge and Gotschalk (1988) (Eq. 1).

The Stokes' Law is only valid at low Reynolds number (Re) in the laminar flow regime, empirically found at Re<0.5 (White, 1974). The Reynolds number is:

$$Re = \frac{\varrho_{sw} W(d_i/10^6)}{\eta} \quad (6)$$

where ϱ_{sw} is the density of seawater (unit: kg/m^3). With the consideration of increasing porosity with size, however, Stokes' Law is potentially valid at higher Reynolds numbers ($1< Re < 50$) (Laurenceau-Cornec et al., 2020). Indeed, roller-tank aggregates with minerals were best modelled using Stokes' Law with constant porosity (99%), and also well described with a form of Stokes' Law modified with a fractal-porosity relationship (Laurenceau-Cornec et al., 2020), similar to our Eq. 5. However, for aggregates without minerals, the modified Stokes' law with the fractal-porosity relationship modelled the sinking velocity much better than using constant porosity. Even though the observation was not based on naturally formed marine aggregates, it is still our best understanding of the applicability of Stokes' Law to marine particles, and we use Eq. 5 to estimate sinking velocities of our natural mineral-containing particles. It is noteworthy that the fractal-porosity relationship for natural marine aggregates used in this study (Eq. 2) has a lower coefficient but similar fractal dimension compared to artificial aggregates in Laurenceau-Cornec et al. (2020). Lower coefficients can be visualized with Figure 2, where natural aggregates seem to have a lower intercept than roller tanks aggregates.

2.3.1 Particle density calculation

Major phases in marine particles include particulate organic matter (POM), opal, lithogenic materials (Litho), calcium carbonate ($CaCO_3$), manganese oxides (MnO_2), and iron oxyhydroxides ($Fe(OH)_3$). The contribution of each particle phase to the overall particle mass, known as the compositional fraction, is calculated by normalizing its concentration with suspended particulate mass (SPM). Compositional fractions in the LSF and SSF are calculated separately and used in the calculations of particle density. The density of the solid portion of particles, $\varrho_{particle}$, is calculated as:

$$\varrho_{particle}=\varrho_{POM}f_{POM}+\varrho_{opal}f_{opal}+\varrho_{Litho}f_{Litho}+\varrho_{CaCO_3}f_{CaCO_3}+\varrho_{MnO_2}f_{MnO_2}+\varrho_{Fe(OH)_3}f_{Fe(OH)_3} \quad (7)$$

where ϱ_{POM}, ϱ_{opal}, ϱ_{Litho}, ϱ_{CaCO_3}, ϱ_{MnO_2}, $\varrho_{Fe(OH)_3}$ are the densities of each particle phase, and f_{POM}, f_{opal}, f_{Litho}, f_{CaCO_3}, f_{MnO_2}, $f_{Fe(OH)_3}$ are the compositional fractions (by weight) of each particle phase. We use a density of POM ϱ_{POM} of 1.05 g/cm^3 (Young, 1994), ϱ_{opal} of 2.0 g/cm^3 (Hurd & Theyer, 1977), ϱ_{Litho} of 2.70 g/cm^3 (Rixen et al., 2019), ϱ_{CaCO_3} of 2.71 g/cm^3, ϱ_{MnO_2} of 3.0 g/cm^3, and $\varrho_{Fe(OH)_3}$ of 3.96 g/cm^3 (Towe & Bradley, 1967).

2.3.2 Hydrography

Hydrographic data, such as temperature, salinity, dissolved oxygen, and nutrients, were measured in each cruise (Cutter et al., 2019; Schlitzer et al., 2018). The potential density was calculated using the seawater toolbox version 3.3.1 in MATLAB (MathWorks Inc.). Temperature, salinity, and pressure from the bottle data were interpolated linearly to pump depths. The seawater density is a function of temperature, salinity, and pressure, and the gravitational acceleration was derived from latitude and depth. The seawater viscosity was calculated from temperature and salinity based on the equation in Millero (1974).

2.3.3 Data binning

Both SSF (1-51 μm) and LSF (>51 μm) are evenly divided into 25 bins in logarithmic space. Since particles of more than 5 mm are generally rare in the ocean (Honjo et al., 1995; Shanks & Trent, 1980), we set the upper limit of the LSF to 5 mm. The size range and median for each size bin are summarized in Table S2. The center of the bin in log space is used in the calculation of sinking speeds and mass fluxes. Since we only have bulk composition information available for the SSF and LSF fractions, we assume that all 25 bins in each size fraction have the same particle composition, and thereby the same particle densities.

2.4 Mass-size spectra

A mass-size spectrum is calculated for each sample in all cruises using the measured bulk SSF and LSF SPM concentrations. All spectra are assumed to be a power function between 1 μm and 5 mm. LSF and SSF SPM concentrations, together with size boundaries in different size fractions, 1, 51 and 5000 μm, were used to constrain the relationships:

$$m_i=pd_i^{-q} \quad (8)$$

$$SPM=\frac{\int_{d_1}^{d_2} pd_i^{-q}dd}{10^3} \quad (9)$$

where m_i is the dry mass of particles for each bin i (unit: g/L/m), SPM is the measured dry suspended particulate mass in each size fraction (unit: g/m^3), 10^3 is the conversion factor between μg/L and g/m^3, d_1 is the lower integration boundary, as 1 μm in the SSF or 51 μm in the LSF, d_2 is the higher integration boundary, as 51 or 5000 μm, and p and q are constant parameters that are determined from the size-fractionated SPM data for each sample. The coefficient q is unitless.

2.5 Mass flux calculation

The mass flux is obtained from the product of SPM concentrations and sinking velocities. The mass flux for each size bin, F_i, is calculated as:

$$F_i=\frac{m_i \times W_i}{10^3} \tag{10}$$

where F_i is with the unit of $g/m^2/s/\mu m$, and 10^3 is the conversion factor between μm and mm. The overall mass flux F is the sum of mass fluxes in all size bins:

$$F=\int_{d_1}^{d_2} \frac{m_i \times W_i}{10^3} dd \tag{11}$$

where F is with the unit of $g/m^2/s$. To convert $g/m^2/s$ to $g/m^2/day$, one needs to multiply by 86400 s/day. The SSF and LSF mass flux are calculated separately for each sample. The total mass flux is the sum of SSF and LSF fluxes.

2.6 Mass-weighted average sinking velocity calculation

The calculation of the mass-weighted average sinking velocity for the SSF and LSF size fractions uses the mass fraction of each size bin to weight the velocity calculated in each size bin. The mass-weighted average sinking velocity WSV (unit: m/s) is computed separately for the SSF (1-51 μm), the LSF (51-5000 μm), and total particles (1-5000 μm) as:

$$WSV=\int_{d_1}^{d_2} \frac{m_i W_i dd}{\int_{d_1}^{d_2} m_i dd} \tag{12}$$

Indeed, the mass flux F of the SSF, LSF, or total particles is the product of the WSV multiplied by SPM concentrations of the respective size fraction:

$$F=WSV \times SPM \tag{13}$$

Derived mass flux and WSV in all size fractions (SSF, LSF, and TOT) from three cruises are summarized in Table S3.

2.7 Statistical Analysis

In this paper, two methods of statistical tests are conducted to evaluate whether variables in three oceans are significantly different. The choice of the statistical method depends on the distribution for given datasets. The normality of data distribution is assessed using the Lilliefors test at the 5% significance level. We use the two-sample t-test (α=0.05) to examine statistical differences between variables if they both have a normal distribution. Otherwise, the Wilcoxon rank sum test, known as the Mann-Whitey U test, is used. Most of our derived parameters are not normally distributed. Unless otherwise specified, the p value shown is from the Wilcoxon rank sum test.

3. Results

3.1 Suspended Particulate Mass (SPM)

LSF, SSF, and total (TOT) SPM concentrations in three basins tend to decrease with depth (Figure S1). In general, the SPM is of higher concentrations in the SSF than LSF (see section 3.4.1). The Chukchi Shelf in the western Arctic Ocean has the highest SPM concentrations in all size fractions, reaching 1.1, 3.2, and 4.0 g/m^3 for the LSF, SSF, and TOT, respectively, approached only by the bottom nepheloid layer of the western boundary current in the North Atlantic from the GA03 cruise. In contrast, the Canada Basin of the western Arctic Ocean is characterized by the lowest SPM concentrations in the LSF ($p<<0.001$). The SSF and TOT SPM concentrations in the western Arctic Ocean and SE Pacific central basin are not statistically different from each other ($p>0.05$) but are both significantly smaller than the North Atlantic ($p<<0.001$). Interestingly, most deviations between the North Atlantic and SE Pacific occur in the deep ocean: there is less SPM attenuation with depth in the North Atlantic. Inputs from hydrothermal vents are responsible for the small elevation in SPM concentrations at 2500 m in the EPR 15˚S hydrothermal plume in the SE Pacific. The North Atlantic western boundary has much more prominent bottom nepheloid layers (BNLs) than the SE Pacific or Arctic, as found by Gardner et al. (2018a), Gardner et al. (2018b), and Gardner et al. (2018c).

3.2 Compositional Fraction

The LSF and SSF particles have different particle compositions, with their POM and opal fractions differing the most. In general, the LSF POM is less dominant than the SSF, whereas the LSF opal fraction is greater than in the SSF (Figures S2g-j & S3). The POM is the dominant particle phase in the upper 500 m in both size fractions and the fraction of POM decreases with depth in all three basins. In contrast, the fraction of lithogenic material progressively increases with depth (Figures S2e-f & S3). The particulate lithogenic content in the SE Pacific is significantly smaller than that in the Arctic and North Atlantic ($p<<0.001$). Unlike the North Atlantic, which is heavily influenced by Saharan dust input (e.g., Mahowald et al., 2005), the western Arctic Ocean is far from major dust sources, and the supply of lithogenic aerosol particles into the Arctic Ocean is much smaller (Marsay et al., 2018). The central Arctic Basin receives most of its lithogenic material via lateral fluxes from the margins (Xiang & Lam, 2020). Prominent bottom nepheloid layers in the North Atlantic and the western Arctic Ocean are characterized by high lithogenic fractions, accounting for over 60% of the SPM. $CaCO_3$, a biogenic mineral of similar density to lithogenic particles (see section 2.3.1), is highest in the SE Pacific ($p<<0.001$) and lowest in the Arctic Ocean in both size fractions ($p<<0.001$). The abundance of $CaCO_3$ compensates for a lack of lithogenic particles in the SE Pacific, leading to relatively similar fractions of Litho+$CaCO_3$ in the three ocean basins (Figure S2c-f). The North Atlantic has the lowest fraction opal ($p<<0.001$). High opal fractions are observed in the SE Pacific and western Arctic Ocean, whereas a more definite decreasing trend with depth appears in the western Arctic Ocean (Figures S2g-h & S3). The $Fe(OH)_3$ is generally low but elevated in the EPR 15˚S and TAG hydrothermal plumes where the highest fraction of $Fe(OH)_3$+MnO_2 consists of up to 60% of SPM (Figure S2a-b). Despite the absence of hydrothermal activities, the western Arctic Ocean is the only basin with a relatively high fraction of MnO_2 (>2%) in the entire water column (Figure S3). The highest fraction in the SSF (~9%) is found in the upper 500 m in the western Arctic Ocean coinciding with the Pacific-derived halocline, and is even higher than that in the EPR hydrothermal plume. There is no obvious MnO_2 elevation in the TAG plume, despite similar dissolved manganese concentrations between the EPR 15˚S and TAG plumes (Hatta et al., 2015; Resing et al., 2015); therefore, the presence of high concentration and fraction of MnO_2 in the EPR 15˚S but not in the TAG (Lam et al., 2018; Lam et al., 2015) is likely a consequence of the comparative

ages of the plumes relative to the time scale of dissolved Mn oxidation (Kipp et al., 2018; Mandernack & Tebo, 1993).

3.3 Particle densities and excess densities

Particle densities range from 1.1 to 3.2 g/cm^3 in the three sections and generally increase with depth (Figure 3). The highest density is found in the EPR 15° S hydrothermal plume. The median for LSF particle densities is 1.8, 2.0, and 2.0 g/cm^3 in the North Atlantic, SE Pacific, and the western Arctic Ocean, respectively. The SSF densities are 2.0±0.4, 1.9±0.4, and 1.9±0.4 g/cm^3 (mean±s.d.). Based on the Lilliefors test, only LSF densities in the North Atlantic are normally distributed at the 5% significance level. In contrast, all SSF particle densities have normal distributions. The North Atlantic has the lowest LSF densities compared to the other two cruises ($p<<0.001$), but its SSF densities are significantly higher than the western Arctic Ocean (t-test; $p<0.01$). Such contrasting characteristics between size fractions can be partly explained by the abundance of POM and the lack of opal in the North Atlantic in the LSF (Figures S2g, S2i, &S3).

Both the magnitude and variations of seawater densities are small compared to the particle density in most cases, which leads to relatively consistent differences between particle density and excess densities (Figure S4). Variations in the excess density are controlled by composition effects on particle density, not by variations in the seawater density.

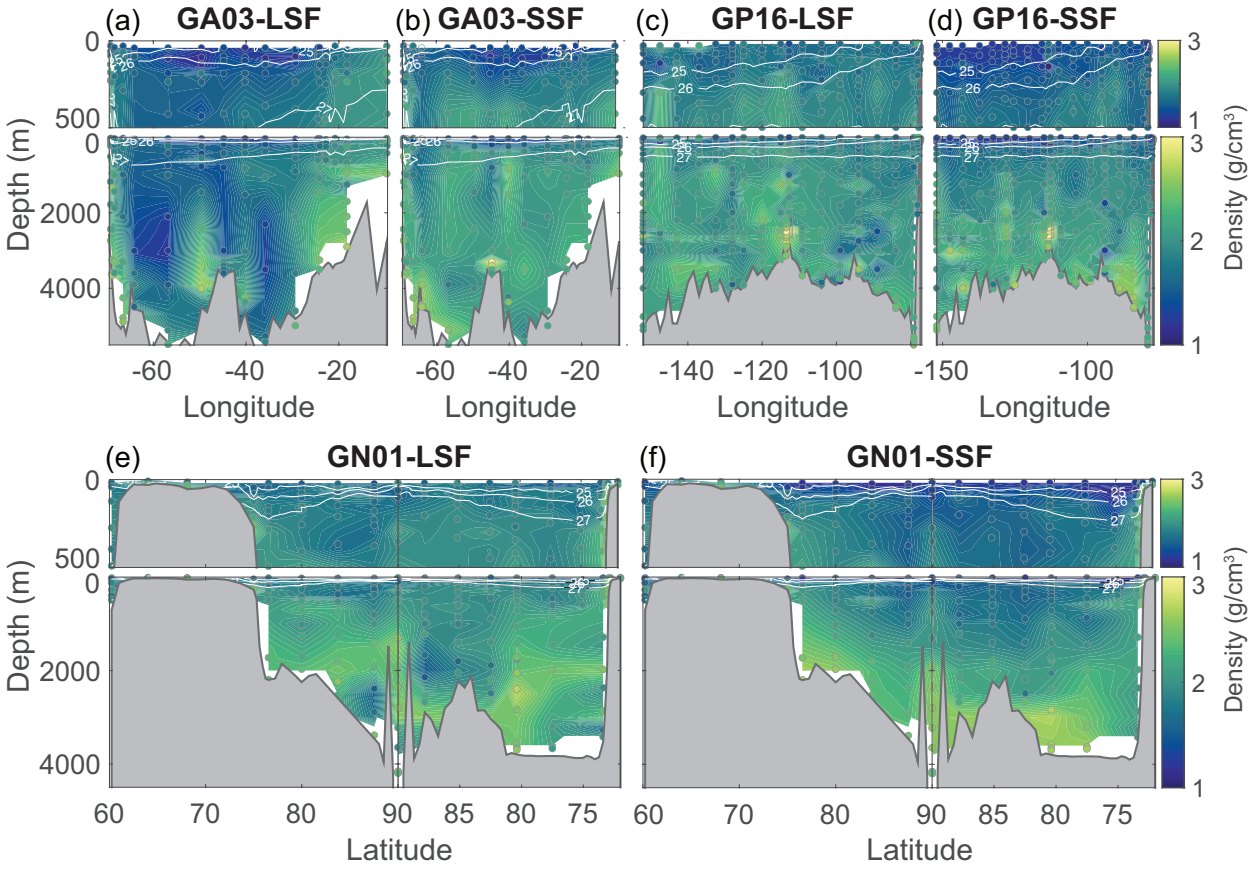

Figure 3. LSF (>51 μm) and SSF (1-51 μm) particle densities (unit: g/cm^3) in three cruises. (a): GA03 LSF; (b): GA03 SSF; (c): GP16 LSF; (d): GP16 SSF; (e) GN01 LSF; (f): GN01 SSF. The top panel in each subplot is the upper 500 m, and the lower panel is the entire water column. Pump

sampling depths with actual data are shown with colored dots outlined in gray, on top of interpolated values that are plotted on model grids. Both actual and interpolated values are assigned with the same color bar. Thick white contours are potential density anomaly of 25, 26 and 27 kg/m^3, and thin white lines are 50 evenly spaced contour lines within the range of the color scale. In GN01, northbound and southbound legs are connected, and the North Pole station (90˚N) is shown in the center.

3.4 Mass partitioning

3.4.1 The fraction of mass concentrations in the SSF and LSF

The SSF SPM generally makes up more TOT SPM concentrations than the LSF (Figure 4). A higher fraction of small particles with respect to total mass concentrations (fSSF) corresponds to a higher power q in the mass-size spectra. The median (range) fSSF fractions are 76.6% (34.2-97.8%), 78.4% (48.4-93.9%), and 85.5% (11.1-96.5%) in the North Atlantic, SE Pacific, and the western Arctic Ocean, respectively. The highest fSSF of 97.8% appears in the BNLs along the western boundary in the North Atlantic (Figure 4a). Close to the venting site of the EPR hydrothermal plume, the fSSF is about 70%, implying hydrothermal particles from the EPR partition less towards the SSF than outside the plume (Figure 4b) (Lee et al., 2018). The central Arctic Basin is characterized by significantly higher fSSF (more small particles) than the North Atlantic and SE Pacific ($p<<0.001$) (Figure 4c), consistent with oligotrophic conditions and subsurface lateral transport of fine particles in the western Arctic Ocean (Xiang & Lam, 2020). Interestingly, the lowest fSSF and thereby the largest particles are also in the western Arctic Ocean, but over the productive Chukchi Shelf (Figure 4c).

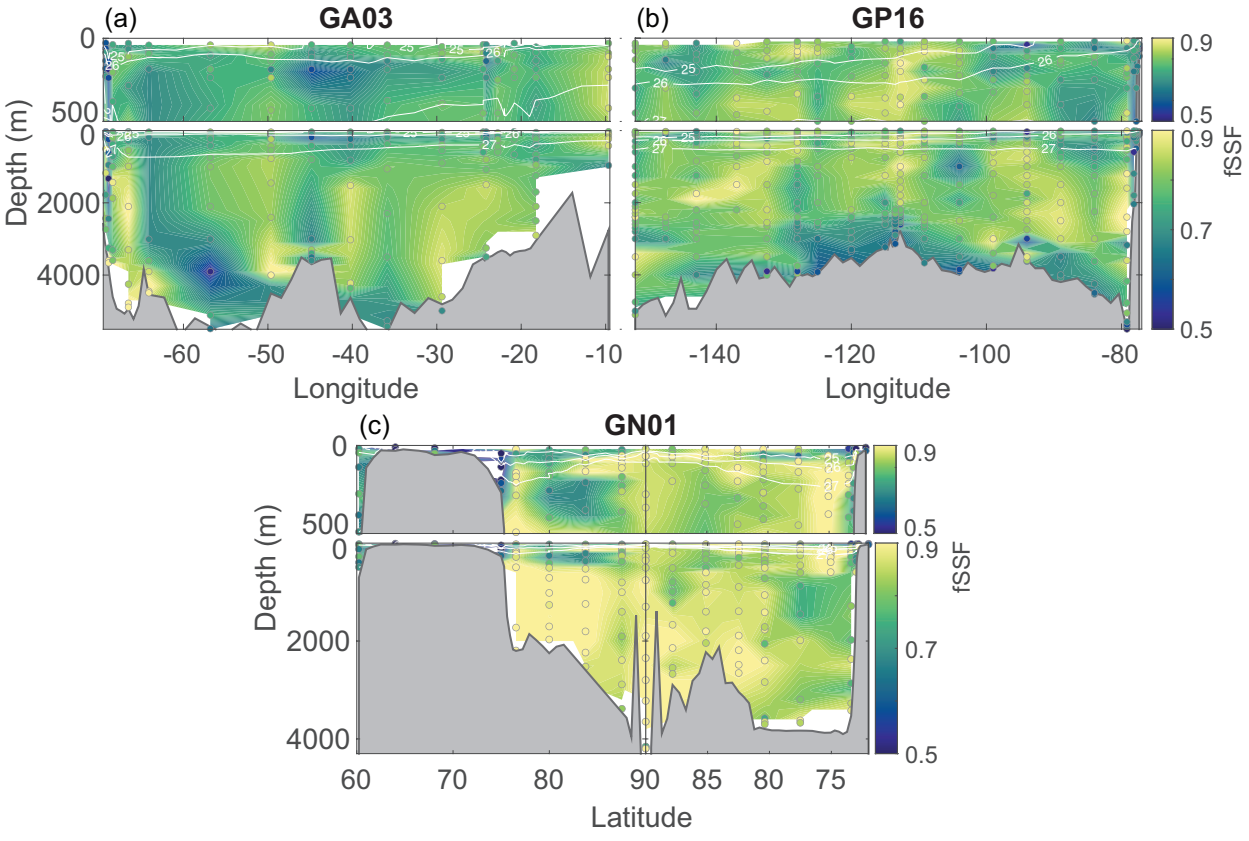

Figure 4. Fraction of SSF in TOT (>1 μm) mass concentrations in three cruises. (a): GA03; (b): GP16; (c) GN01. The top panels in each subplot is the upper 500 m, and the lower panel is the entire water column.

3.4.2 The mass-size spectra power q

Another means to assess the mass partitioning in size-fractionated particles is to compare the magnitude of the power q in the mass-size spectra (Eq. 8). A higher q indicates more mass distributed to the SSF compared to the LSF. The mass-size spectra formulation also facilitates subsequent calculations of sinking velocities (see section 2.6). The distributions of the two parameters, fSSF and q, look alike (Figures 4 & S5). The medians (ranges) of q are 1.3 (0.9-2.0), 1.3 (1.0-1.7), 1.5 (0.6-1.8) in the North Atlantic, SE Pacific, and the western Arctic Ocean, respectively.

3.5 Derived variables

3.5.1 Derived mass flux

The LSF mass flux generally decreases with depth and away from the margins, with values ranging over three to four orders of magnitude within each cruise. The medians (5^{th} to 95^{th} percentile range) of LSF mass flux are 2.0×10^{-1} g/m^2/d (2.1×10^{-2}-1.9 g/m^2/d) in the North Atlantic, 8.9×10^{-2} g/m^2/d (2.3×10^{-2}-1.0 g/m^2/d) in the SE Pacific, and 4.4×10^{-2} g/m^2/d (8.2×10^{-3}-8.7 g/m^2/d) in the western Arctic Ocean (Figure S6). In terms of 0-100% range of mass flux over all cruises, it is worth noting that samples with the highest (88.2 g/m^2/d) and lowest (2.9×10^{-3} g/m^2/d) mass flux are both in the western Arctic Ocean. The BNLs along the western boundary in the North Atlantic increase the LSF mass flux to about 3.5 g/m^2/d. In the SSF, the mass flux varies one to two orders of magnitude within each cruise. The medians (5^{th}-95^{th}) of SSF mass flux are 1.6×10^{-2} g/m^2/d (4.5×10^{-3}-8.3×10^{-2} g/m^2/d) in the North Atlantic, 6.5×10^{-3} g/m^2/d (2.7×10^{-3}-4.4×10^{-2} g/m^2/d) in the SE Pacific, and 4.9×10^{-3} g/m^2/d (1.5×10^{-3}-2.7×10^{-1} g/m^2/d) in the western Arctic Ocean (Figure S6). Fluxes of more than 1.0 g/m^2/d are rare in the SSF, only occurring in prominent BNLs, such as on the western margin in the North Atlantic and the Chukchi Shelf in the western Arctic Ocean.

The distribution of TOT mass fluxes is similar to the LSF (Figures 5 & S6). The medians (5^{th}-95^{th}) of TOT mass flux are 2.1×10^{-1} g/m^2/d (2.5×10^{-2}-2.5 g/m^2/d) in the North Atlantic, 9.7×10^{-2} g/m^2/d (2.7×10^{-2}-1.1 g/m^2/d) in the SE Pacific, and 4.9×10^{-2} g/m^2/d (1.1×10^{-2}-9.6 g/m^2/d) in the western Arctic Ocean (Figure 5). The highest (100^{th} percentile) TOT mass flux is over the Chukchi Shelf, reaching 89.6 g/m^2/d. The North Atlantic is characterized by the highest TOT mass flux (Figure 5a), and the western Arctic Ocean has the lowest TOT mass flux ($p<<0.001$) (Figure 5e). It is interesting that high mass fluxes in the upper 500 m near the Peru margin persist hundreds of kilometers offshore in the SE Pacific, coinciding with the 10 μmol/kg dissolved oxygen contour line (Figure 5c). The low attenuation of mass flux in this region is consistent with conclusions drawn from other tracers from the same cruise, such as the ^{230}Th-normalized POC flux and stable isotope of nitrate ($\delta^{15}N_{NO3}$), which both point to less POC regeneration within the Peru oxygen deficient zone (Pavia et al., 2019; Peters et al., 2018).

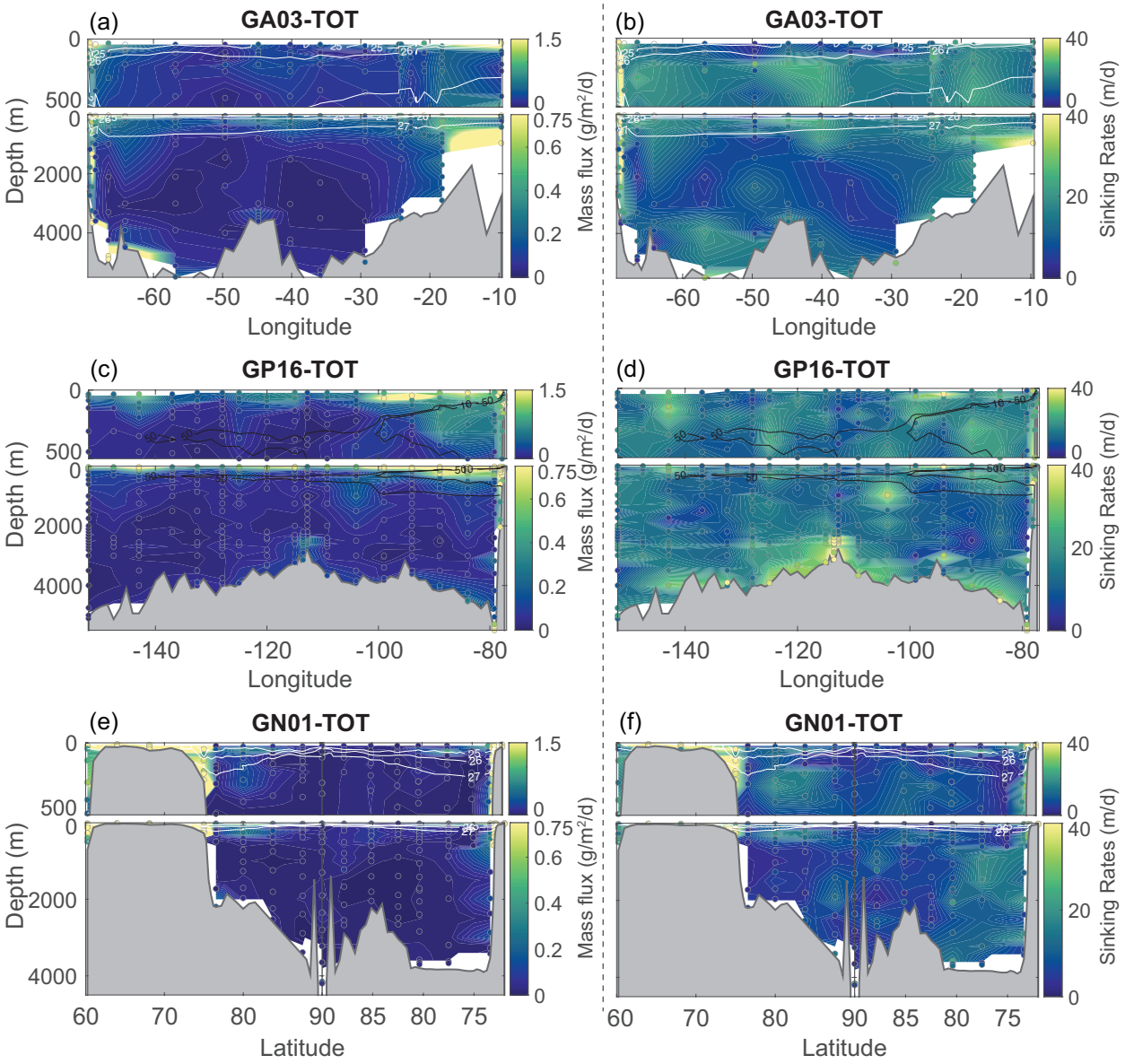

Figure 5. Derived mass flux (unit: g/m^2/d) in TOT particles (a, c, e), and derived mass-weighted average sinking velocity (unit: m/d) in TOT particles in three cruises (b, e, f). (a)-(b): GA03; (c)-(d): GP16; (e)-(f): GN01. Thick white contours are potential density anomaly of 25, 26 and 27 kg/m^3, and thick black contours in the GP16 are dissolved oxygen concentrations of 10 and 50 μmol/kg. Note that color scales are the same for all cruises but are different between the upper 500 m (top panels) and the whole water column (bottom panels) in the TOT mass flux.

3.5.2 Derived mass-weighted average sinking velocities

The magnitude of mass-weighted average sinking velocities (WSVs) for each size fraction is determined by the mass fraction and sinking velocity for each size bin (Eq. 12). Sinking velocities, in turn, are dependent on the hydrography, particle composition, and porosity-size relationship. The medians (5th-95th range) of WSVs over all cruises are 60.6 m/d (27.0-103.8 m/d) in the LSF, and 1.4 m/d (4.1×10^{-1}-2.6 m/d) in the SSF (Figure S7). Unlike the mass flux, where the total flux was similar to the LSF flux, WSVs in total particles are less similar to the LSF WSVs:

the TOT sinking rates fall between the SSF and LSF, with the median (5^{th}-95^{th}) of 13.5 m/d (3.4-41.0 m/d) (Figure 5). This is because the WSVs are an average sinking speed weighted by mass, thus giving more weight to the slowly sinking particles of the more abundant SSF. In contrast, flux is simply integrated across sizes, and the larger size range and faster sinking speeds of the LSF dominate the total flux. In general, we did not find strong evidence for an increasing sinking velocity with depth, in line with observations by Xue and Armstrong (2009) and Nowald et al. (2009).

The LSF WSVs are high near shelf/slope regions in the North Atlantic, but relatively low in the surface and deep basin (Figure S7a). The SE Pacific has relatively uniform distributions of LSF WSVs (Figure S7c). The median (5^{th}-95^{th}) of LSF WSVs in the SE Pacific is 65.7 m/d (42.8-113.0 m/d), not significantly different from the North Atlantic ($p>0.05$), which has the median (5^{th}-95^{th}) of 62.9 m/d (19.5-118.3 m/d). Interestingly, despite having significantly higher LSF particle densities compared to the North Atlantic, the Arctic Ocean is characterized by the lowest LSF sinking rates in all three basins ($p<<0.001$) (Figure S7e). The median (5^{th}-95^{th}) in the LSF in the western Arctic Ocean is 46.1 m/d (23.3-90.5 m/d). In this case, the smaller particle size distribution (Figures 4&S5) and greater importance of viscosity relative to gravitational sinking (see section 4.3.2.2) in the western Arctic Ocean may play a more important role in diminishing sinking velocity.

Similar to the LSF, the western Arctic Ocean is also characterized by the lowest WSVs in the SSF ($p<<0.001$), and the median (5^{th}-95^{th}) is 1.0 m/d (2.4×10^{-1}-2.1 m/d) (Figure S7f). However, unlike for the LSF, the SSF WSVs are relatively high in the deep North Atlantic compared to the other basins (Figure S7b). The SSF WSVs in the SE Pacific (median: 1.4 m/d; 5^{th}-95^{th}: 6.4×10^{-1}-2.7 m/d) are significantly lower than the North Atlantic (median: 1.7 m/d; 5^{th}-95^{th}: 8.8×10^{-1}-2.7 m/d) ($p<<0.001$) (Figure S7d).

The median (5^{th}-95^{th}) of TOT WSVs is 15.4 (4.1-52.2 m/d), 15.2 (6.6-37.0 m/d), and 7.4 m/d (2.3-39.1 m/d) in the North Atlantic, SE Pacific, and the western Arctic Ocean, respectively (Figure 5). In the central North Atlantic, the TOT WSVs have surface and deep minima of less than 10 m/d (Figure 5b). As a consequence of a dominance of very small particles in the BNLs, the TOT WSVs along the deep western boundary are lower than the midwater column values despite much higher fractions of lithogenic contents. Within the near-field EPR hydrothermal plume (<80 km from the ridge axis) in the SE Pacific, the TOT WSVs can reach more than 50 m/d (Figure 5d) owing to increasing particle densities (Figure 3b) from the high oxide fraction (Figure S2a-b) and lower fSSF (more large particles) (Figure 4b). The most pronounced gradient in TOT WSVs between the shelf/slope and basin is observed in the western Arctic Ocean (Figure 5f). Overall, the TOT WSVs in the western Arctic Ocean are significantly lower than the other two oceans ($p<<0.001$).

4. Discussion

4.1 Sensitivity tests

Sensitivity tests are conducted with different numbers of size bins, upper size limits for the LSF, and porosity-size relationships. Compared to the latter two, the number of bins is of minor importance in the variations of mass flux and WSVs, and not discussed here. Additionally, according to Eq. 13, for given SPM concentrations, the variability is the same between mass flux and WSVs. Therefore, we only discuss changes in the mass flux term in sensitivity tests below.

The mass-size spectra (Eq. 8) change slightly with different upper size limits in the LSF. The difference in the power q is generally <1.5% if 10 mm is used as the upper size boundary instead of 5 mm. However, mass flux is sensitive to the variations in the upper limit in the LSF. Using the data from the SE Pacific as an example, if setting the upper size boundary as 10 mm rather than 5 mm, the TOT mass flux and WSVs are both elevated. The absolute difference ranges from 1.4×10^{-3} to 1.9 g/m^2/d and the median is 3.0×10^{-2} g/m^2/d (Figure S8a). The percentage of increase has a median (range) of 30.1% (4.3%-58.9%).

The mass flux is also very sensitive to the choice of the porosity-size relationship. As seen in Figure 2, the power-law relationship in the Alldredge and Gotschalk (1988) (P1) has a steeper slope and higher coefficient than the new compilation used in this paper (P2). For particle sizes below 5 mm, the P1 relationship tends to have a higher 1-P, thereby lower P, which leads to higher mass fluxes. If keeping the upper size limit in the LSF as 5 mm, the TOT mass flux derived from the P1 changes by a median of 1.5×10^{-1} g/m^2/d and 156.7% in the absolute and relative increase, respectively, when compared to ones calculated using the P2 relationship (Figure S8b).

4.2 Literature comparisons

Most observations of mass fluxes are from sediment traps. Particles collected by sediment traps and large-volume in-situ pumps, however, integrate over different temporal and spatial scales. Moored sediment traps are usually deployed for weeks and months, neutrally buoyant or surface-drifting traps are deployed for days, whereas pumps collect particles for several hours. Longer deployment times allow sediment traps to capture rare fast-sinking particles, but sediment traps tend to undercollect slowly-sinking particles owing to hydrodynamic discrimination (Gustafsson et al., 2004). Pumps sample abundant slowly-sinking particles well, but are less likely to capture rare, fast-sinking particles. Despite the sampling differences, derived TOT mass fluxes using the pump data in this study are comparable to existing sediment trap studies (Figure 6) (Berelson et al., 2015; Honjo et al., 1995; Honjo et al., 2010; Hwang et al., 2015; Torres-Valdés et al., 2014). Note that there are fewer sediment trap studies in the South Pacific and Arctic Oceans as there are in the North Atlantic. Mass fluxes derived from the newly compiled P2 porosity-size power function are closer to sediment trap observations than those using the original P1 relationship. The difference in mass flux between the two porosity-size relationships results from higher porosity for all particles >8.6 μm in the P2 relationship, given an upper size limit of 5 mm in our current study.

Existing measurements of sinking velocities of natural marine particles, direct or indirect, vary by several orders of magnitude, ranging from several meters to thousands of meters per day (Alldredge & Gotschalk, 1988; Alonso-González et al., 2010; Armstrong et al., 2009; Bach et al., 2016; Bach et al., 2019; Berelson, 2001; Briggs et al., 2020; Estapa et al., 2019; Giering et al., 2016; McDonnell & Buesseler, 2010; McDonnell & Buesseler, 2012; Nowald et al., 2009; Peterson et al., 2005; Pilskaln et al., 1998; Riley et al., 2012; Trull et al., 2008; Turner, 2002). Our estimates of TOT WSVs, about 10-30 m/d (Figure 5), fall within the range of 2 to 54 m/d measured using gel traps and in situ camera system for particles between 73 and 1400 μm at the Bermuda Atlantic Time-Series (BATS) in the Sargasso Sea (McDonnell & Buesseler, 2012). The TOT WSVs, however, are almost an order of magnitude higher than 2-3 m/d estimated using a thorium (Th) based inverse method in the North Atlantic (Lerner et al., 2017). Approximations of the sinking velocity derived from ^{230}Th observations are also about 1-3 m/d in other parts of the ocean (Bacon & Anderson, 1982; Krishnaswami et al., 1981; Rutgers van der Loeff & Berger, 1993; Scholten et al., 1995). Puigcorbé et al. (2015) estimated the sinking velocity of total particles as

5±2 m/d based on ^{234}Th data collected with pumps in the Northeast Pacific. In general, the SSF WSVs (~1-3 m/d) are much closer to the values from these Th-based estimates compared to the TOT WSVs (~10-30 m/d). Burd et al. (2007) pointed out that bulk measurements such as particulate ^{234}Th are likely to represent the properties of small particles more than large particles. Adsorption of radionuclides such as thorium is a function of available particle surface area (e.g., Santschi et al., 2006), and should thus be weighted to small particles that have higher surface area to volume ratios. In contrast, in our method, mass flux and WSVs are both mass-based and derived from the particle volume (Eqs. 11&12), which gives more importance to larger particles and thus a higher total sinking velocity.

Alternative chemical tracers, such as chloropigments, have also been used with inverse models to calculate sinking velocities for different size pools. Indeed, sinking rate estimates from a recent chloropigments-based inverse method by Wang et al. (2019) using data from in-situ pumps in the Mediterranean Sea are in good agreement with our study. Their modeled sinking velocities are 66.8±68.6 m/d (mean±s.d.) for large particles (>70 μm), with a range between 7 to 183 m/d, and 1.8±1.9 m/d, for small particles (1-70 μm), ranging between 0.2-5 m/d.

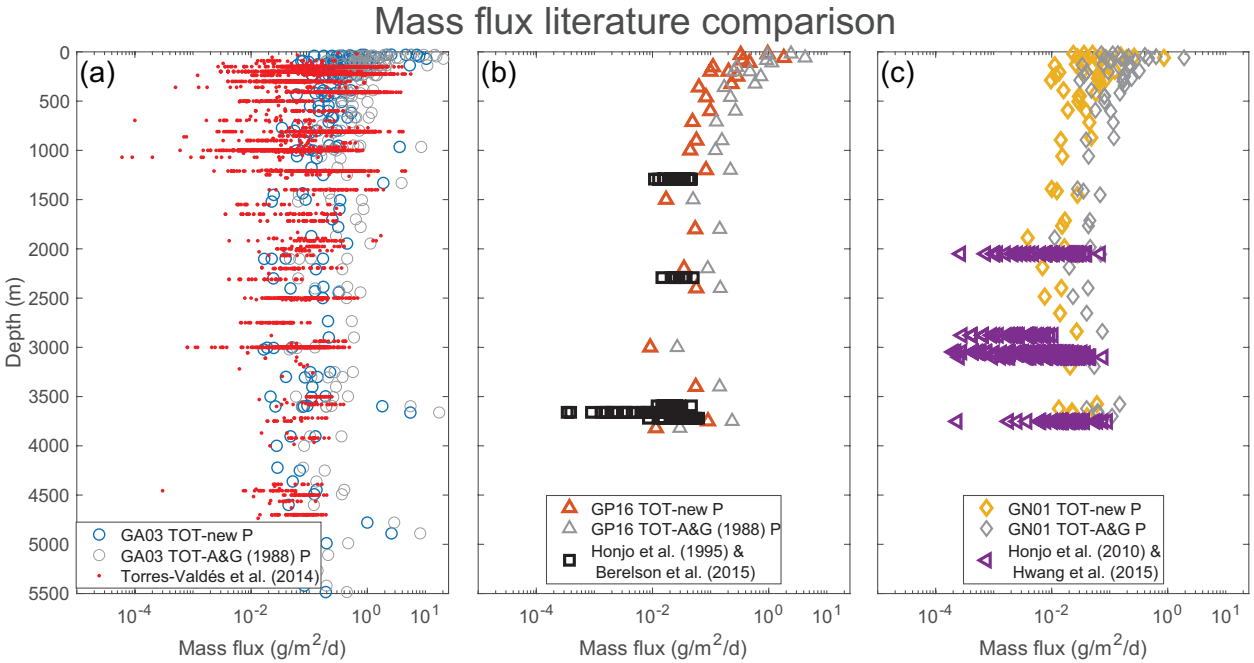

Figure 6. Comparisons between pump-derived and sediment trap-measured TOT mass flux (unit: g/m^2/d) in three cruises. (a): GA03; (b): GP16; (c): GN01. Mass fluxes calculated from the porosity-size relationship in Alldredge and Gotschalk (1988) are in gray. All GA03 stations are used to compared with data from Torres-Valdés et al. (2014), which covers both North and South Atlantic and includes many types of sediment traps. Only Stations 13-14 and 29-30 in the GP16 are used in (b) to compare with Station 12 in Honjo et al. (1995) and Stations 5 and 7 in Berelson et al. (2015). The TOT mass flux in Stations 46-56 in the Canada Basin in the GN01 are shown in (c). Sediment traps in both Honjo et al. (2010) and Hwang et al. (2015) were deployed at 75°N, 150°W in the center of Canada Basin.

4.3 Controls on the mass flux

The mass flux is calculated as the product of the particle concentration and sinking velocity. Sinking velocity, in turn, depends on composition, size, and hydrography (g, viscosity, and seawater density). Previous work has mostly focused on different factors impacting particle sinking velocities, such as the role of particle size (Alldredge & Gotschalk, 1988; Engel et al., 2009; Guidi et al., 2008; Iversen & Ploug, 2010; Iversen & Robert, 2015; Laurenceau-Cornec et al., 2020; Laurenceau-Cornec et al., 2015b; McDonnell & Buesseler, 2010; Schmidt et al., 2014), particle composition (Bach et al., 2016; Bach et al., 2019; Engel et al., 2009; Laurenceau-Cornec et al., 2020; Laurenceau-Cornec et al., 2015b; Schmidt et al., 2014), and the hydrographic effects owing to the density discontinuities (Alldredge et al., 2002; Alldredge & Crocker, 1995; Kindler et al., 2010; MacIntyre et al., 1995; Prairie et al., 2013; Prairie et al., 2015). Our comprehensive work examines all of these components governing the mass flux and adds valuable in-situ particle composition data to the existing literature.

4.3.1 Effects of particle concentration and weighted sinking velocities on mass flux

The SPM concentrations and weighted sinking velocities are used to calculate the mass flux (Eq. 13). Of these two factors, the mass flux is better correlated with SPM than with WSVs (Figure 7), with the relationships best for the LSF.

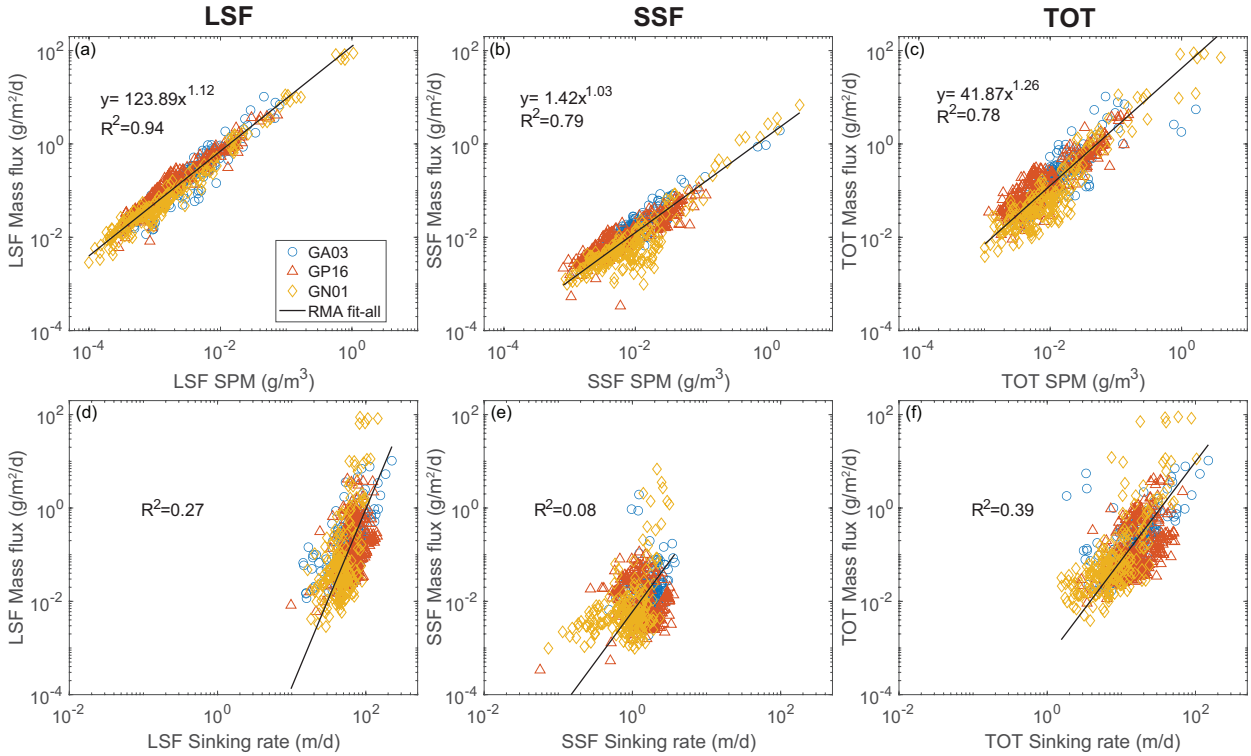

Figure 7. Relationships between size-fractionated SPM concentrations and mass flux (a-c), and between mass-weighted average sinking velocity (WSVs) and mass flux (d-f). The (a) and (d) are LSF, (b) and (e) are SSF, (c) and (f) are TOT. All the x and y are in logarithmic scale. The reduced major axis (Model II linear fit) is used in the regression. Regression equations are displayed in (a)-(c), whereas only the coefficient of determination R^2 is shown in (d)-(f). All regression fits are significant (F-test: degrees of freedom: ~700, $p<0.001$).

The scatter about the relationship between mass flux and SPM reflects the influence of WSV and therefore in the components (particle composition, size, and hydrography) that contribute to WSV. The scatter is most evident at the low end in the western Arctic Ocean in the SSF and TOT. The sections below will discuss how particle size, composition, and hydrography affects the sinking velocity and thus the mass flux.

4.3.1.1 Effects of particle size on sinking velocity

It is straightforward to recognize the importance of size in controlling the sinking velocity: according to Stokes' Law, sinking velocities increase with the square of particle diameter. The size effect on sinking velocity is highly dependent on the porosity-size relationship, however. Incorporation of any porosity-size relationship reduces the exponent value in Stokes' Law (Eqs. 3-4), diminishing the importance of particle size. The lower coefficient in the newly compiled porosity-size relationship increases the importance of porosity for particles as small as 8.6 μm, which tends to reduce overall sinking velocities and thus flux compared to the porosity-size relationship from Alldredge and Gotschalk (1988) (Figure 6). The integration of the new porosity-size relationship (Figure 2) results in a power of ~0.8 applied to particle diameter, which makes the dependence of sinking velocity less sensitive to changes in size than to changes in density.

Additionally, much lower mass partitioning to large particles further reduces the significance of particle size on sinking velocity. In our model, the mass fraction decreases with size due to a negative slope between the mass concentration and size (Eq. 9 & Figure S5). The WSVs are the sum of sinking velocity in each size bin weighted by its mass fraction (Eq. 12). With porosity, the last LSF size bin (4.2×10^3-5.0×10^3 μm) has sinking velocities of about four orders of magnitude higher than the first bin in the SSF (1.0-1.2 μm), reaching a median of 3.5×10^2 m/d. Its mass fraction, however, is much lower and only accounts for a median of 0.35% in TOT mass concentrations. Therefore, the effects of particle size on the overall mass flux are much less important than the classic perspective from Stokes' Law, due to the existence of porosity, as also proposed by Laurenceau-Cornec et al. (2020), and the dominance of smaller particles.

4.3.1.2 Effects of particle composition on sinking velocity

Several previous studies have shown that incorporation of minerals, such as lithogenic particles and $CaCO_3$, decreases particle size (De La Rocha et al., 2008; Engel et al., 2009; Hamm, 2002; Iversen & Ploug, 2010; Laurenceau-Cornec et al., 2020; Nowald et al., 2015; Passow & De La Rocha, 2006; Passow et al., 2014; Schmidt et al., 2014). Most of these conclusions were drawn using aggregates formed in lab roller tanks. Natural aggregates may have different behaviors when exposed to minerals.

In our study using natural particles from the full water column, we did not find evidence to support the role of $CaCO_3$ and opal in affecting particle size distribution (Figure 8a-b & e-f). We do find, however, that the abundance of small particles (denoted by the magnitude of the exponent q) decreases with lithogenic fraction (Figure 8c-d). This relationship is predominantly driven by particles in the deep western Arctic Ocean and by the strong bottom nepheloid layers (BNLs) of the western boundary current in the North Atlantic and Chukchi Shelf (Lam et al., 2015; Xiang & Lam, 2020). The western Arctic Ocean is heavily influenced by lateral transport from sediment resuspension over the Chukchi Shelf and Slope, resulting in high fractions of lithogenic particles below 1000 m (Xiang & Lam, 2020). The association of lithogenic content and small particle size is thus driven by sediment resuspension processes, and not by a decrease in aggregate size caused by lithogenic content. If we exclude the entire GN01, small particles in the North Atlantic and SE

Pacific outside strong BNLs no longer decrease with the lithogenic fraction (Figure 8i-j). Indeed, the abundance of large particles may even increase with the SSF lithogenic fractions. Therefore, we postulate that in areas away from sediment resuspension, incorporation of ballast minerals into aggregates is not a primary controlling factor on the particle size distribution.

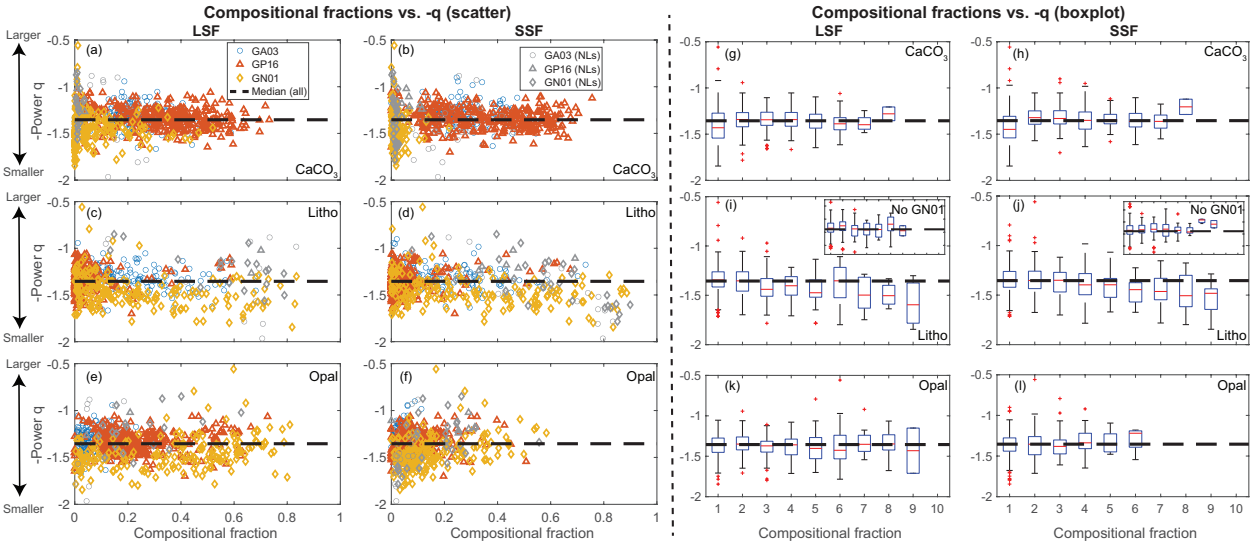

Figure 8. Scatter (a-f) and box plots (g-l) between size-fractionated (LSF: left; SSF: right) compositional fraction and negative power exponent q, -q, in the mass-size spectra. Three major ballast minerals, $CaCO_3$, Litho and opal, are shown in the top, middle and bottom panels, respectively. The black dashed line is the median of all -q in each size fraction from all cruises. Nepheloid layers (NLs) are defined as any lithogenic concentrations of >5 μg/L in both size fractions and plotted in gray in the scatter plots. Compositional fractions are binned for every 10% between 0 and 100% in the box plots, excluding all NLs samples. The red segment inside the rectangle indicates the median and whiskers above and below the box show values of the minimum and maximum. Outliers are shown with red plus signs. Insets in (i) and (j) are plots excluding data from the GN01.

The sinking velocity increases with excess densities on the basis of Stokes' Law. The densities of $Fe(OH)_3$ and MnO_2 are higher than $CaCO_3$ and lithogenic materials, but they are usually a much smaller fraction of the particulate mass (Figures S2-3). A few notable exceptions occur in hydrothermal plumes, where they can account for up to 50% of SPM concentrations. The $CaCO_3$ and Litho are often the most important ballast minerals owing to their high densities and abundances. The density of POM (~1.05 g/cm^3) is the lowest among all major phases and similar to seawater density (~1.03 g/cm^3). Given the small value in the excess density, particles with a high fraction of POM sink slowly compared to other types.

It is worth noting that the opal density, ~2.0 g/cm^3, is very similar to the median of overall particle densities in the ocean (see section 3.3), which tend to frequently be a mixture of POM and $CaCO_3$ and/or Litho. Additions of opal into marine aggregates would not lead to substantial increases in excess densities, thereby sinking velocities, and suggest that opal is likely of minor importance in influencing the overall sinking velocity. To increase sinking velocities, particles have to be characterized by elevated fractions of $Fe(OH)_3$, MnO_2, $CaCO_3$ or Litho. Our hypothesis is consistent with Klaas and Archer (2002) where they explain the low correlation between deep

POC and opal fluxes as a consequence of the relatively low density of opal compared to $CaCO_3$ and lithogenic particles. The apparent weak ballasting effect of opal has also been attributed to higher aggregate porosities, reduced aggregate compactness, and increased POC lability (Bach et al., 2016; Bach et al., 2019; Francois et al., 2002; Lam & Bishop, 2007; Lam et al., 2011). This work shows that an increase in the fraction of opal is not associated with a higher abundance of larger particles (Figure 8e-f & k-l). Direct measurements of opal size and porosity in the future are needed to examine the role of porosity in the opal ballast more carefully.

To summarize, we did not observe any obvious decrease in particle size distribution with incorporation of ballast minerals in natural particles. In this study, effects of particle composition mainly manifest in density of different phases, where $CaCO_3$ and lithogenic particles are generally the two most important ballast minerals that add excess density to POM. The direct ballast effect of opal appears to be very weak, given its similar density to median of particle densities. We cannot exclude other hypotheses for the weak role of opal in particle flux, such as ecosystem effects (Lima et al., 2014) and POC lability (Lam et al., 2011), however.

4.3.1.3 Effects of hydrography on sinking velocity

Hydrographic parameters in the Stokes' velocity calculation include seawater density, gravitational acceleration, and viscosity. Strong density gradients appear in the upper water column in three oceans, especially in the Arctic Ocean. A decrease in sinking velocities and accumulations of particles within a thin layer of sharp density gradients has been observed for marine aggregates both in-situ and in laboratory settings (Alldredge et al., 2002; Alldredge & Crocker, 1995; Kindler et al., 2010; MacIntyre et al., 1995; Prairie et al., 2013; Prairie et al., 2015). Elevations of beam attenuation from the transmissometer are generally observed within the pycnocline in all three cruises (Anderson & Fleisher, 2013). Our pump sampling resolution, however, may not be fine enough to capture such features on the scale of a few meters, given the absence of obvious elevations in particle concentrations at the density discontinuities.

The influence of seawater density is incorporated into the calculation of excess densities, but as noted previously, variations in seawater density are usually small compared to variation in particles densities (see section 3.3). Sharp density gradients are generally associated with sharp viscosity gradients, since both parameters depend on temperature and salinity, so the hydrography effects on mass flux mainly manifest in the g/viscosity term (Eq. 3). Gravitational acceleration varies by less than 1% between Arctic and tropical waters. The most variation results from the viscosity, which is highly temperature-dependent (Millero, 1974). We disregard potential biological contributions to viscosity such as from the release of mucous materials including transparent exopolymer particles (TEP) (Jenkinson, 1986; 1993; Jenkinson & Biddanda, 1995; Seuront et al., 2007; Seuront et al., 2010; Seuront & Vincent, 2008; Seuront et al., 2006).

In the western Arctic Ocean, the ratios of g/viscosity (g/vis) are lowest in the surface (~5000 m^2/s/kg), highest at about 300 m below the Pacific-derived halocline (~5400 m^2/s/kg), and remain relatively constant in the deep ocean (~5200 m^2/s/kg) (Figure 9). In contrast, g/vis ratios are highest in the surface North Atlantic and SE Pacific (~10000 m^2/s/kg), and decrease rapidly with depth. Higher values of g/vis in the surface (low viscosity) facilitate particle sinking out of the surface where remineralization rates are highest. On the basis of g/viscosity profiles alone, one would expect sinking velocities to slow down with depth in the North Atlantic and SE Pacific, especially in upper 2000 m, whereas not change much in the western Arctic Ocean. The fact that WSVs do not decrease with depth in the North Atlantic and SE Pacific (Figures 5b, 5d, & S7a-d) is caused by generally increasing excess densities with depth (Figure 3). Places with small

g/viscosity variations with depth, such as the western Arctic Ocean, however, have more potential for increasing excess density to increase sinking velocities with depth.

When comparing values of g/vis between three basins, they only differ by <10% in the deep ocean, but can be up to 200% different in the upper water column (Figure 9). This distinct feature in the high-latitude Arctic Ocean can lead to up to two times smaller sinking velocities and mass fluxes than low-latitude oceans, partly contributing to smaller sinking velocities and mass fluxes in the upper water column in the Arctic Ocean (Figures S6-S7).

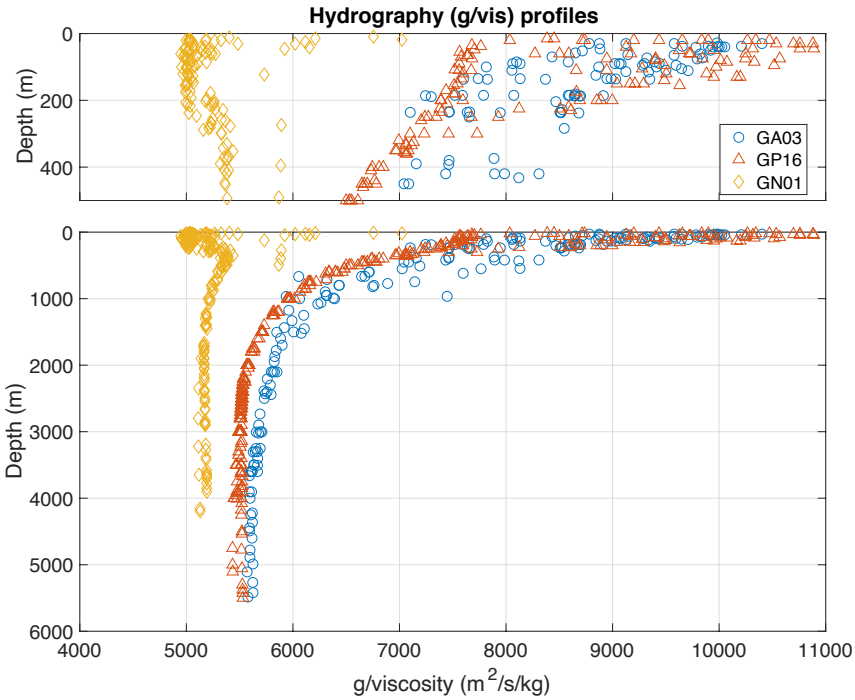

Figure 9. Profiles of hydrographic parameter g/ viscosity (unit: $m^2/s/kg$) in the upper 500 m (top panel) and the whole water column (bottom panel) in three cruises.

4.3.2 The relative importance of hydrography, particle concentration, size, and composition for mass flux

The size-fractionated mass flux is calculated as the sum of mass flux in each size bin (Eq. 11). Equivalently, it can also be expressed as the product of the overall mass concentration and WSVs (Eq. 13). Combining Eqs. 4, 12 and 13, we generate an overall equation with concentration, size, composition, and hydrography terms to calculate mass flux (Eq. 14), which can be used to quantitatively de-convolve the contribution of each effect to the variability and magnitude of mass flux in the SSF and LSF (Table 1).

$$F=\left(\int_{d_1}^{d_2}\frac{m_i}{\int_{d_1}^{d_2} m_i dd}\times(1-P_i)\frac{g\Delta\rho(d_i/10^6)^2}{18\eta}dd\right)\times SPM \quad (14)$$

We define the concentration effect directly as SPM, and the size effect as $\int_{d_1}^{d_2}\frac{m_i}{\int_{d_1}^{d_2} m_i dd}\times(1-P_i)\times(d_i/10^6)^2 dd) = \int_{d_1}^{d_2}\frac{m_i}{\int_{d_1}^{d_2} m_i dd}\times 3.6\times10^{-11.4}\times(d_i)^{0.8}dd$, which includes both the porosity-size relationship and mass partitioning of particles, and is calculated as the sum of contribution from

each size bin. The excess density, $\Delta\varrho$, is used to represent the composition effect, and the hydrography effect is defined as g/viscosity, g/η. Multiplying all four terms would generate an adjusted mass flux that is 18 times higher than the actual derived mass flux (unit: g/m^2/s). The variability and magnitude of individual terms, therefore, are helpful in understanding their relative importance in determining mass flux. We only focus on the upper 100 m of the water column of all non-shelf stations to assess the importance of these four effects across surface ecosystems. To avoid extreme outliers, we use the range between 5 and 95 percentiles in each term to demonstrate the variability and magnitude of mass flux.

Table 1. *The Contributions from Different Factors to the Variation of Mass Flux (<100 m)*

Cruise	Effects	LSF		SSF	
		5-95%ile range (median)	95/5 range ratios	5-95%ile range (median)	95/5 range ratios
GA03	Concentration [unit: g/m^3]	4.1×10^{-3}-6.3×10^{-2} (7.5×10^{-3})	15.5	1.4×10^{-2}-4.7×10^{-2} (2.5×10^{-2})	3.4
	Size [unit: m^2]	2.0×10^{-9}-3.8×10^{-9} (2.4×10^{-9})	1.9	4.9×10^{-11}-9.2×10^{-11} (5.9×10^{-11})	1.9
	Composition [unit: kg/m^3]	1.5×10^{2}-9.5×10^{2} (4.9×10^{2})	6.3	2.5×10^{2}-9.0×10^{2} (4.5×10^{2})	3.5
	Hydrography [unit: m^2/s/kg]	8.1×10^{3}-1.0×10^{4} (9.4×10^{3})	1.3	8.1×10^{3}-1.0×10^{4} (9.4×10^{3})	1.3
GP16	Concentration [unit: g/m^3]	2.6×10^{-3}-2.3×10^{-2} (7.7×10^{-3})	9.1	1.7×10^{-2}-5.9×10^{-2} (2.9×10^{-2})	3.5
	Size [unit: m^2]	1.7×10^{-9}-2.7×10^{-9} (2.2×10^{-9})	1.6	4.1×10^{-11}-6.6×10^{-11} (5.3×10^{-11})	1.6
	Composition [unit: kg/m^3]	4.9×10^{2}-1.2×10^{3} (6.5×10^{2})	2.4	2.1×10^{2}-5.9×10^{2} (3.1×10^{2})	2.8
	Hydrography [unit: m^2/s/kg]	7.7×10^{3}-1.1×10^{4} (9.7×10^{3})	1.4	7.7×10^{3}-1.1×10^{4} (9.7×10^{3})	1.4
GN01	Concentration [unit: g/m^3]	8.7×10^{-4}-3.9×10^{-2} (3.0×10^{-3})	44.8	8.4×10^{-3}-8.6×10^{-2} (1.5×10^{-2})	10.2
	Size [unit: m^2]	1.4×10^{-9}-3.1×10^{-9} (2.0×10^{-9})	2.2	3.3×10^{-11}-7.6×10^{-11} (4.9×10^{-11})	2.3
	Composition [unit: kg/m^3]	4.2×10^{2}-1.3×10^{3} (6.8×10^{2})	3.0	1.3×10^{2}-9.3×10^{2} (2.9×10^{2})	7.0
	Hydrography [unit: m^2/s/kg]	5.0×10^{3}-5.3×10^{3} (5.1×10^{3})	1.1	5.0×10^{3}-5.3×10^{3} (5.1×10^{3})	1.1
Global	Concentration [unit: g/m^3]	9.8×10^{-4}-4.1×10^{-2} (6.5×10^{-3})	42.1	9.3×10^{-3}-5.3×10^{-2} (2.4×10^{-2})	5.7
	Size [unit: m^2]	1.6×10^{-9}-3.2×10^{-9} (2.3×10^{-9})	2.0	3.9×10^{-11}-7.7×10^{-11} (5.5×10^{-11})	2.0
	Composition [unit: kg/m^3]	2.8×10^{2}-1.1×10^{3} (6.5×10^{2})	4.1	1.6×10^{2}-7.7×10^{2} (3.5×10^{2})	4.9
	Hydrography [unit: m^2/s/kg]	5.0×10^{3}-1.1×10^{4} (8.9×10^{3})	2.1	5.0×10^{3}-1.1×10^{4} (8.9×10^{3})	2.1

4.3.2.1 Effects on variability of mass flux

The variability of mass flux within each size fraction with respect to hydrography, particle concentration, size, and composition is first evaluated by examining the ratio of the 95th to 5th percentile values for each of these four effects as defined above (Table 1). This 95th to 5th

percentile ratio is a metric we use to quantify the observed variability in these effects, and thus assess the expected influence each effect may have on the observed variability in mass flux.

SPM shows the highest ratio of the 95^{th} to 5^{th} percentiles in all three cruises, and thus accounts for most of the variability in the mass flux, consistent with good correlations between SPM concentration and mass flux (Figures 7a-c, 10a-b). The concentration range ratio in the western Arctic Ocean (44.8 and 10.2 for LSF and SSF, respectively) is much higher than other oceans, demonstrating the enormous SPM range sampled on that cruise (Figure 10a-b). Given the much higher SPM concentrations on the Chukchi Slope, we also calculated the ratio between 90 and 5 percentiles for both size fractions in the western Arctic Ocean, and they are 19.2 and 3.0 for the LSF and SSF, respectively. The adjusted LSF ratio in the western Arctic Ocean is still the highest among all cruises, whereas the SSF is similar to the North Atlantic and SE Pacific.

The composition effect has the second highest ratio of the 95^{th} to 5^{th} percentiles. In the North Atlantic, the SSF range ratio for composition is slightly higher than that in the concentration. Particle composition differences may thus be more important than concentration differences for explaining mass flux variability in the SSF.

Surprisingly, the range of variability as a result of the size effect is relatively low in both size fractions, about 1-3 times lower than the composition effect. Despite the strong d_i^2 size dependence in the size term in the Stokes equation, the incorporation of size-dependent porosity reduces this effect to a dependency on $d_i^{0.8}$. Furthermore, not only are larger particles more porous, but they are less abundant than smaller particles (see section 4.3.1.1). Therefore, when comparing the sinking velocity from different locations in the SSF or LSF, samples with a high fSSF (more abundant small particles) do not necessarily correspond to slower sinking velocities because the composition effect can predominate over the size effect. Indeed, the ratio of 95^{th} to 5^{th} percentiles is greater for the composition effect than for the size effect in all cruises, demonstrating that there are greater variations in particle density than in particle size distributions.

The hydrography effect generally has lower 95^{th} to 5^{th} percentile ratios than the size effect. The largest difference between the size and hydrography effects occurs in the western Arctic Ocean, due to a combination of increased variability in size and decreased hydrography effect compared to other oceans.

On a global scale including all three cruises, the concentration effect still leads to most variability in the mass flux in the upper 100 m and the composition effect is the second most important term (Table 1). The high 95^{th} to 5^{th} percentile ratio for the concentration effect is driven by the very low (5^{th} percentile) concentrations in the western Arctic Ocean (Figure 10a-b). The LSF concentration range is more variable than the SSF, whereas the SSF excess density range is more pronounced than the LSF (Table 1). SSF mass flux increases with excess density (Figure 10 b&d). LSF mass flux appears to have little relationship with excess density, until one notices that the GA03 and GP16 data do have a relationship, but the GN01 samples from the western Arctic cluster in a range of relatively high excess density but low mass flux and WSVs (Figure 10 a&c). This is explained by the influence of the significantly smaller particle size distribution and particle concentrations, and most viscous water in the Arctic compared to the North Atlantic and SE Pacific. The relatively similar range ratios between the SSF composition and concentration effects lead to less scatter in the overall relationship of excess density *vs*. mass flux than the LSF. Additionally, the ratio of 95^{th} to 5^{th} percentiles for the hydrography effect on a global scale is almost two times higher than that on a regional scale, due to contrasting hydrographic features

between polar and tropical oceans (Figure 9), which makes the ratio very similar to the size effect (Table 1).

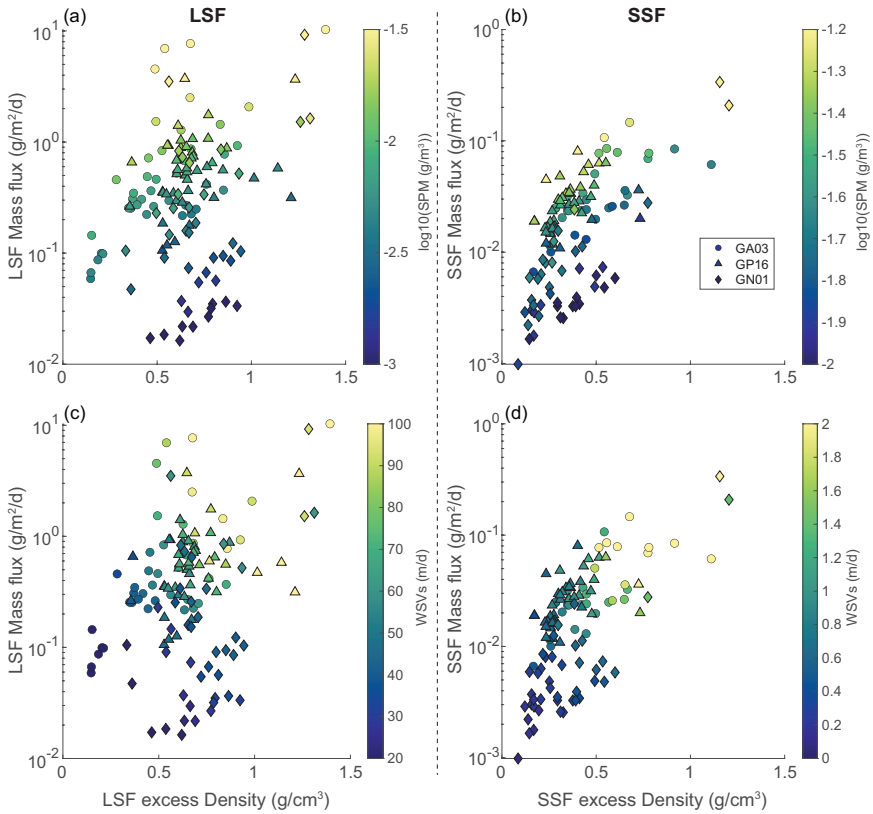

Figure 10. Scatter plots between size-fractionated (LSF: left; SSF: right) excess density and mass flux in the upper 100 m of all non-shelf stations (bottom depth>200 m). The color bars are log10(SPM) on the top row (a-b), and mass-weighted average sinking velocity (WSVs) on the second row (c-d). Note that the y axes and color bar for SPM are in logarithmic scale.

4.3.2.2 Effects on magnitude of mass flux

We are also interested in addressing two questions related to the magnitude of mass flux: 1) why is the magnitude of LSF mass flux smallest in the central basin of western Arctic Ocean? 2) why do LSF particles dominate the TOT mass flux throughout the water column even though they have much smaller mass concentrations than the SSF?

First, we assess the difference in magnitudes between four terms in the upper 100 m across all cruises. Since the LSF consists of the majority of TOT mass flux, we only discuss LSF flux here. The LSF mass flux in the upper 100 m in the western Arctic Ocean is significantly smaller than the other two oceans ($p<<0.001$). Indeed, the magnitudes of the concentration and hydrography effects are smallest in the western Arctic Ocean (<100 m) ($p<<0.001$), and the size effect in the western Arctic Ocean is similar to the SE Pacific ($p>0.05$) but both are smaller than the North Atlantic ($p<0.01$). In contrast, the LSF excess density in the western Arctic Ocean is significantly larger than the North Atlantic ($p<0.01$) and similar to the SE Pacific ($p>0.05$). The slightly higher excess density in the western Arctic Ocean compared to the North Atlantic (median excess density in the LSF is 0.7 and 0.5 g/cm^3 in the western Arctic Ocean and North Atlantic, respectively) cannot compensate for smaller size and hydrography effects, resulting in the smallest

LSF WSVs in the upper 100m in the western Arctic (median: 37.8 m/d; p<<0.001; Figure 10c). The much lower LSF SPM concentrations in the western Arctic Ocean further decrease the mass flux (Figure 10a). Therefore, the lowest mass fluxes in the western Arctic Ocean are not due to a lack of ballast minerals as proposed by (Honjo et al., 2010), but rather to a combination of smallest particle sizes, lowest particle concentrations and most viscous water (lower g/vis). This conclusion also holds true for the rest of the water column.

Secondly, high values of mass flux for LSF compared to SSF result from their much higher sinking velocities than the SSF (Eq. 13). Indeed, we can determine quantitatively which term (size, composition or hydrography) is the main driver elevating sinking velocity over the entire water column. Based on our definition of size effect, the ratios of size effect between LSF and SSF can be calculated as: $\frac{\int_{51}^{5000}\frac{m_i}{\int_{51}^{5000}m_i dd}\times(1-P_i)\times(d_i/10^6)^2 dd}{\int_{1}^{51}\frac{m_i}{\int_{1}^{51}m_i dd}\times(1-P_i)\times(d_i/10^6)^2 dd}$, which is relatively constant, ~41. Given that the ratio of the concentration effect between LSF and SSF over all cruises has a median (5^{th}-95^{th} percentile range) of 0.3 (0.1-0.8), the size alone can more than compensate for lower concentrations in the LSF and lead to higher mass flux. Additionally, the LSF excess densities are slightly higher than the SSF in the upper 100 m (Figure 10): the median (5^{th}-95^{th}) ratio of the composition effect between LSF and SSF is 1.8 (0.7-4.8). Since both size fractions experience the same hydrographic parameters, it is the larger particle sizes and, to a lesser degree, denser particles in the LSF that explain the dominance of this size fraction's contribution to the total mass flux.

4.3.2.3 Overall dependency of mass flux on particle size

Since m_i, P_i and Wi are functions of d_i in Eq. 14, we can further substitute Eqs. 2 and 8 into 14 and derive the overall dependency of F on d_i:

$$F=3.6\times10^{-14.4}\times\frac{p\times\Delta\varrho\times g}{18\eta}\times\int_{d_1}^{d_2}(d_i)^{0.8-q}dd \quad (15)$$

The integrated mass flux F is calculated using the mass flux spectrum integrated over a size interval $[d_1, d_2]$. We simplify Eq. 15 and define the mass flux as $F=\int_{d_1}^{d_2} f(d)dd$. The mass flux spectrum f(d) is a power function with positive coefficients and an exponent of 0.8-q. For any given particle size, the values of f(d) are always positive, which leads to positive flux F for any size interval.

The median (5^{th}-95^{th}) of mass-size spectra power q over all three cruises is 1.4 (1.1-1.6). Accordingly, the power of f(d) has a median (5^{th} to 95^{th}) of -0.6 (-0.8 to -0.3). Therefore, the mass flux spectrum generally has a negative slope, and the function f(d) decreases with size. The negative sign of the power signifies that the mass flux in any single size bin generally decreases as a function of particle size, similar to the mass-size and number-size spectra, although the absolute magnitude of the power in the mass flux spectrum is much smaller. Noticeably, in some rare cases, the mass flux spectrum can even have a positive slope and increase with size. Over the Chukchi Shelf in the western Arctic Ocean, there are very low q values (denoted larger particles), reaching as low as 0.6 (Figure S5), which leads to a positive exponent 0.2 in f(d).

4.4 Key assumptions and their limitations

This study relies on several key assumptions: (1) the mass concentration and size follow a power-law relationship; (2) a power function also describes the relationship between porosity and

907 size; (3) the particle composition is the same across the size spectrum within each size fraction for
908 a specific sample; (4) the sinking of particles obeys Stokes' Law. We examine each of these
909 assumptions.
910 First, due to the difficulties of observing individual particle mass directly, there is not much
911 direct evidence for the application of a single power-law relationship between mass concentration
912 and size. The mass size distribution in this study was derived from bulk measurements of particle
913 mass in two size fractions. Its power law form assumes that the higher abundance of small particles,
914 as confirmed by numerous optical observations of the number size spectrum (e.g., Jackson et al.,
915 1997; Loisel et al., 2006; Roullier et al., 2014; Stemmann et al., 2008; Stemmann et al., 2004),
916 overcomes the greater mass for individual large aggregates, giving rise to a negative slope between
917 the mass concentration and size. Indeed, our data confirm that the mass of particles in the SSF is
918 almost always larger than in the LSF. Applying a single slope to the entire size range is likely an
919 oversimplification for the complex natural assemblage of particles, but hopefully captures the first
920 order distribution of mass.
921 Secondly, the single power-law function between the porosity and size used in this work is
922 also a simplification of the myriad controls on porosity. Compared to the original equation in
923 Alldredge and Gotschalk (1988), the updated power law in this study incorporates more data
924 points, especially in the smaller end of the size range, as well as different methods for estimating
925 particle porosities. As discussed above in section 4.1, the derived mass flux is quite sensitive to
926 the choice of porosity-size relationship. More data points are needed in future studies, especially
927 in size range of 0.3 to 1.0 mm (Figure 2). It is clear from the considerable scatter in both the
928 original and updated relationships that there are many more controls on porosity than size alone.
929 Given the many mechanisms that produce marine aggregates, including abiotic coagulation and
930 fecal pellet production by a wide variety of animals, it is probable that better estimates of mass
931 fluxes require multiple power functions or a more complicated non-linear relationship.
932 Thirdly, different particle types (Andrews et al., 2010; Reynolds et al., 2016; Woźniak et
933 al., 2010), and phytoplankton communities (Green et al., 2003a; Green et al., 2003b; Smyth et al.,
934 2019; Stramski et al., 2001) have distinct size distributions, and their corresponding peaks in
935 particle number concentrations do not often occur at the same size. For example, relatively dense
936 lithogenic particles and $CaCO_3$ coccoliths are likely concentrated in the smaller end of the SSF
937 spectrum (e.g., Baumann & Sprengel, 2000; Rea & Hovan, 1995) rather than distributed evenly
938 throughout. Thus, the assumption of constant composition in all size bins within each size fraction
939 necessarily results in monotonic changes in sinking velocity with size in the LSF or SSF that might
940 not exist in reality. Using an average bulk composition would lead to an overestimate of true mass
941 flux if denser particle phases were skewed to smaller particles. Since measuring particle
942 composition at each size bin is not practical due to sampling and analytical limitations, we apply
943 two different densities to the size range within the LSF and SSF, respectively, to estimate the mass
944 flux. A similar strategy using a single bulk composition was employed by Bach et al. (2016) when
945 calculating the sinking velocity of natural marine aggregates in mesocosms.
946 Fourthly, the assumption of spherical particles for our Stokes' Law calculations is a
947 simplification, as marine aggregates are not perfect spheres (e.g., Alldredge & Gotschalk, 1988;
948 Engel et al., 2009; McDonnell & Buesseler, 2010). Given the same size and excess density,
949 irregularly shaped aggregates are characterized by lower sinking velocities than spherical ones due
950 to the increased drag (Alldredge & Gotschalk, 1988). Another assumption we made in Stokes'
951 Law calculation is that the flow through the porous aggregate is negligible in order to apply Eq.4.
952 The numerical simulations from Kiørboe et al. (2001), however, suggested that flow occurs in a

953 thin layer at the surface of aggregates, which is borne out by oxygen microsensor measurements
954 within aggregates (Ploug et al., 2008b). Additionally, the presence of TEP can also influence the
955 excess density in sinking velocity estimations. Indeed, much of the space in the porous fraction of
956 aggregates can be occupied by TEP (Ploug & Passow, 2007). TEP is operationally defined as >0.4
957 μm particles filtered by polycarbonate filters that stain with Alcian Blue (Alldredge et al., 1993;
958 Passow, 2002). The density of TEP is 0.70-0.84 g/cm^3, lower than seawater (Azetsu-Scott &
959 Passow, 2004). As TEP measurements were not made in our samples, we did not consider its
960 possible influence, but it would be expected to decrease the mass flux estimation.
961
962 **5. Conclusions**
963 Although this study makes several assumptions to convert suspended particle concentration
964 and composition to mass flux, it predicts mass flux values comparable to various sediment traps
965 studies and gives insights into the controls of export flux on a global scale.
966 We compile porosity and size measurements of natural marine aggregates from the
967 literature and use a modified Stokes' law with the fractal-porosity relationship to calculate sinking
968 velocity and mass flux. Noticeably, TOT mass fluxes derived from the newly compiled porosity-
969 size power-law relationship are more similar to sediment trap observations than if we were to use
970 the porosity-size relationship for marine snow aggregates only from Alldredge and Gotschalk
971 (1988). The western Arctic Ocean is characterized by the lowest TOT WSVs and mass fluxes
972 compared to the North Atlantic and SE Pacific. We did not find evidence for a lack of ballast
973 minerals in the western Arctic Ocean as proposed by Honjo et al. (2010) to explain low mass
974 fluxes. Instead, the lowest TOT mass fluxes found in the western Arctic Ocean result from the
975 smallest particle sizes, the lowest particle concentrations and the most viscous water. It does not
976 mean that composition is not important in determining the magnitude of mass flux, but simply that
977 other factors dominate in the western Arctic. Indeed, away from the Arctic, the LSF mass flux
978 generally increases with excess density (Figure 10), though there is no relationship with the
979 prevalence of any specific particle phase (Figure S9).
980 We also compare the relative importance of particle concentration, composition, size and
981 hydrography effects in the variability and magnitude of mass flux on a global scale combing all
982 three cruises. Our data suggest that the variability of mass flux within each size fraction (LSF, SSF
983 or TOT) is controlled mostly by particle concentration and composition, and less so by size and
984 hydrography (Table 1). While large particles will always have a faster sinking velocity than small
985 particles (all else being equal) and thus explain the important contributions of the LSF to the TOT
986 mass flux, the variations in particle size distribution between samples are smaller than the
987 variations in particle density. This highlights the importance of particle composition, not just size
988 distribution, as key parameters for predicting mass flux.
989 The particle size distribution is a parameter measured by optical methods that is
990 increasingly used to study the biological carbon pump in various cruises and autonomous platforms
991 (Picheral et al., 2017), including the *Tara* Ocean expedition (Guidi et al., 2016). The conversion
992 from particle size to flux, however, often lacks any direct or indirect information about particle
993 composition (Giering et al., 2020; Stemmann & Boss, 2012). The poor constraints in particle
994 densities might partly explain the discrepancy between sediment trap-measured and UVP-derived
995 mass fluxes (Fender et al., 2019; Guidi et al., 2008). Compared to traditional geochemistry
996 measurements, however, optical devices such as the UVP have advantages of much higher spatial
997 and temporal resolution. To better constrain UVP-derived mass flux estimates, we recommend
998 pairing optics with measurements of particle composition in future investigations, either by

sampling simultaneously in the same cruise, or referring to historical measurements. The geochemical determination of particle properties serves as a calibration to optical proxies, and helps us further understand the biological carbon pump on a global scale.

Acknowledgments

This work was supported by NSFOCE-1535854 to PJL. We would like to thank all chief scientists and everyone on board in the GA03, GP16, and GN01 U.S. GEOTRACES cruises. Special thanks to all people in the pump group for helping to collect particle samples at sea. We sincerely thank past and current members in the Lam lab for the continuous assistance in both lab work and data analysis, and Thomas Weber and Bo Yang for their help in data visualization. We also thank X anonymous reviewers for their suggestions and comments to improve this manuscript. All size-fractionated particle concentration and composition data described above are available on the Biological and Chemical Oceanography Data Management Office website (GA03: https://www.bco-dmo.org/dataset/3871; GP16: https://www.bco-dmo.org/dataset/668083; GN01: https://www.bco-dmo.org/dataset/807340).

References

Alldredge, A. L., Cowles, T. J., MacIntyre, S., Rines, J. E. B., Donaghay, P. L., Greenlaw, C. F., et al. (2002). Occurrence and mechanisms of formation of a dramatic thin layer of marine snow in a shallow Pacific fjord. *Marine Ecology Progress Series*, *233*, 1-12. doi:10.3354/meps233001

Alldredge, A. L., & Crocker, K. M. (1995). Why do sinking mucilage aggregates accumulate in the water column? *Science of The Total Environment*, *165*(1), 15-22. doi:10.1016/0048-9697(95)04539-D

Alldredge, A. L., & Gotschalk, C. (1988). In situ settling behavior of marine snow. *Limnology and Oceanography*, *33*(3), 339-351. doi:10.4319/lo.1988.33.3.0339

Alldredge, A. L., Passow, U., & Logan, B. E. (1993). The abundance and significance of a class of large, transparent organic particles in the ocean. *Deep Sea Research Part I: Oceanographic Research Papers*, *40*(6), 1131-1140. doi:10.1016/0967-0637(93)90129-Q

Alldredge, A. L., & Silver, M. W. (1988). Characteristics, dynamics and significance of marine snow. *Progress in oceanography*, *20*(1), 41-82. doi:10.1016/0079-6611(88)90053-5

Alonso-González, I. J., Arístegui, J., Lee, C., Sanchez-Vidal, A., Calafat, A., Fabrés, J., et al. (2010). Role of slowly settling particles in the ocean carbon cycle. *Geophysical Research Letters*, *37*(13). doi:10.1029/2010gl043827

Anderson, R. F., & Fleisher, M. Q. (2013). Particle beam attenuation coefficient (Cp) data from ODF (Ocean Data Facility) rosette, R/V Knorr KN199-04, KN204-01 in the Subtropical northern Atlantic Ocean, 2010-2011 (U.S. GEOTRACES NAT project). *Biological and Chemical Oceanography Data Management Office (BCO-DMO)*, *Dataset version 2013-11-05*.

Andrews, S., Nover, D., & Schladow, S. G. (2010). Using laser diffraction data to obtain accurate particle size distributions: the role of particle composition. *Limnology and Oceanography: Methods*, *8*(10), 507-526. doi:10.4319/lom.2010.8.507

Armstrong, R. A., Lee, C., Hedges, J. I., Honjo, S., & Wakeham, S. G. (2001). A new, mechanistic model for organic carbon fluxes in the ocean based on the quantitative association of POC with ballast minerals. *Deep Sea Research Part II: Topical Studies in Oceanography*, *49*(1-3), 219-236. doi:10.1016/S0967-0645(01)00101-1

Armstrong, R. A., Peterson, M. L., Lee, C., & Wakeham, S. G. (2009). Settling velocity spectra and the ballast ratio hypothesis. *Deep Sea Research Part II: Topical Studies in Oceanography*, *56*(18), 1470-1478. doi:10.1016/j.dsr2.2008.11.032

Aumont, O., Van Hulten, M., Roy-Barman, M., Dutay, J. C., Éthé, C., & Gehlen, M. (2017). Variable reactivity of particulate organic matter in a global ocean biogeochemical model. *Biogeosciences*, *14*(9), 2321-2341. doi:10.5194/bg-14-2321-2017

Azetsu-Scott, K., & Passow, U. (2004). Ascending marine particles: Significance of transparent exopolymer particles (TEP) in the upper ocean. *Limnology and Oceanography*, *49*(3), 741-748. doi:10.4319/lo.2004.49.3.0741

Bach, L. T., Boxhammer, T., Larsen, A., Hildebrandt, N., Schulz, K. G., & Riebesell, U. (2016). Influence of plankton community structure on the sinking velocity of marine aggregates. *Global Biogeochemical Cycles*, *30*(8), 1145-1165. doi:10.1002/2016GB005372

Bach, L. T., Stange, P., Taucher, J., Achterberg, E. P., Algueró-Muñiz, M., Horn, H., et al. (2019). The influence of plankton community structure on sinking velocity and remineralization rate of marine aggregates. *Global Biogeochemical Cycles*, *33*(8), 971-994. doi:10.1029/2019gb006256

Bacon, M. P., & Anderson, R. F. (1982). Distribution of thorium isotopes between dissolved and particulate forms in the deep sea. *Journal of Geophysical Research: Oceans*, *87*(C3), 2045-2056. doi:10.1029/JC087iC03p02045

Baumann, K. H., & Sprengel, C. (2000). Morphological variations of selected coccolith species in a sediment trap north of the Canary Islands. *Journal of Nannoplankton Research*, *22*(3), 185-193.

Berelson, W. M. (2001). Particle settling rates increase with depth in the ocean. *Deep Sea Research Part II: Topical Studies in Oceanography*, *49*(1-3), 237-251. doi:10.1016/S0967-0645(01)00102-3

Berelson, W. M., Haskell II, W. Z., Prokopenko, M., Knapp, A. N., Hammond, D. E., Rollins, N., & Capone, D. G. (2015). Biogenic particle flux and benthic remineralization in the Eastern Tropical South Pacific. *Deep Sea Research Part I: Oceanographic Research Papers*, *99*, 23-34. doi:10.1016/j.dsr.2014.12.006

Bishop, J. K. B., Edmond, J. M., Ketten, D. R., Bacon, M. P., & Silker, W. B. (1977). The chemistry, biology, and vertical flux of particulate matter from the upper 400 m of the equatorial Atlantic Ocean. *Deep Sea Research*, *24*(6), 511-548. doi:10.1016/0146-6291(77)90526-4

Bopp, L., Resplandy, L., Orr, J. C., Doney, S. C., Dunne, J. P., Gehlen, M., et al. (2013). Multiple stressors of ocean ecosystems in the 21st century: projections with CMIP5 models. *Biogeosciences*, *10*(10), 6225-6245. doi:10.5194/bg-10-6225-2013

Boyd, P. W., & Trull, T. W. (2007). Understanding the export of biogenic particles in oceanic waters: Is there consensus? *Progress in Oceanography*, *72*(4), 276-312. doi:10.1016/j.pocean.2006.10.007

Briggs, N., Dall'Olmo, G., & Claustre, H. (2020). Major role of particle fragmentation in regulating biological sequestration of CO2 by the oceans. *Science*, *367*(6479), 791-793. doi:10.1126/science.aay1790

Buesseler, K. O., Lamborg, C. H., Boyd, P. W., Lam, P. J., Trull, T. W., Bidigare, R. R., et al. (2007). Revisiting carbon flux through the ocean's twilight zone. *Science*, *316*(5824), 567-570. doi:10.1126/science.1137959

Burd, A. B., Jackson, G. A., & Moran, S. B. (2007). The role of the particle size spectrum in estimating POC fluxes from Th234/U238 disequilibrium. *Deep Sea Research Part I: Oceanographic Research Papers*, *54*(6), 897-918. doi:10.1016/j.dsr.2007.03.006

Cavan, E. L., Henson, S. A., & Boyd, P. W. (2019). The sensitivity of subsurface microbes to ocean warming accentuates future declines in particulate carbon export. *Frontiers in Ecology and Evolution*, *6*, 230. doi:10.3389/fevo.2018.00230

Cutter, G., Kadko, D., & Landing, W. M. (2019). Bottle data from the CTD-ODF carousel on the GEOTRACES Arctic Section cruise (HLY1502) from August to October 2015 (U.S. GEOTRACES Arctic project). *Biological and Chemical Oceanography Data Management Office (BCO-DMO)*, *Dataset version 2019-07-29*. doi:10.1575/1912/bco-dmo.646825.4

De La Rocha, C. L., Nowald, N., & Passow, U. (2008). Interactions between diatom aggregates, minerals, particulate organic carbon, and dissolved organic matter: Further implications for the ballast hypothesis. *Global Biogeochemical Cycles*, *22*(4). doi:10.1029/2007gb003156

Ebersbach, F., & Trull, T. W. (2008). Sinking particle properties from polyacrylamide gels during the KErguelen Ocean and Plateau compared Study (KEOPS): Zooplankton control of carbon export in an area of persistent natural iron inputs in the Southern Ocean. *Limnology and Oceanography*, *53*(1), 212-224. doi:10.4319/lo.2008.53.1.0212

Engel, A., Szlosek, J., Abramson, L., Liu, Z., & Lee, C. (2009). Investigating the effect of ballasting by CaCO3 in Emiliania huxleyi: I. Formation, settling velocities and physical properties of aggregates. *Deep Sea Research Part II: Topical Studies in Oceanography*, *56*(18), 1396-1407. doi:10.1016/j.dsr2.2008.11.027

Estapa, M. L., Feen, M. L., & Breves, E. (2019). Direct observations of biological carbon export from profiling floats in the subtropical North Atlantic. *Global Biogeochemical Cycles*, *33*(3), 282-300. doi:10.1029/2018gb006098

Fender, C. K., Kelly, T. B., Guidi, L., Ohman, M. D., Smith, M. C., & Stukel, M. R. (2019). Investigating particle size-flux relationships and the biological pump across a range of plankton ecosystem states from coastal to oligotrophic. *Frontiers in Marine Science*, *6*(603). doi:10.3389/fmars.2019.00603

Fowler, S. W., & Knauer, G. A. (1986). Role of large particles in the transport of elements and organic compounds through the oceanic water column. *Progress in oceanography*, *16*(3), 147-194. doi:10.1016/0079-6611(86)90032-7

Francois, R., Honjo, S., Krishfield, R., & Manganini, S. (2002). Factors controlling the flux of organic carbon to the bathypelagic zone of the ocean. *Global Biogeochemical Cycles*, *16*(4), 34-31-34-20. doi:10.1029/2001gb001722

Gardner, W. D., Mishonov, A. V., & Richardson, M. J. (2018a). Decadal comparisons of particulate matter in repeat transects in the Atlantic, Pacific, and Indian Ocean Basins. *Geophysical Research Letters*, *45*(1), 277-286. doi:10.1002/2017GL076571

Gardner, W. D., Richardson, M. J., & Mishonov, A. V. (2018b). Global assessment of benthic nepheloid layers and linkage with upper ocean dynamics. *Earth and Planetary Science Letters*, *482*, 126-134. doi:10.1016/j.epsl.2017.11.008

Gardner, W. D., Richardson, M. J., Mishonov, A. V., & Biscaye, P. E. (2018c). Global comparison of benthic nepheloid layers based on 52 years of nephelometer and transmissometer measurements. *Progress in oceanography*, *168*, 100-111. doi:10.1016/j.pocean.2018.09.008

Giering, S. L. C., Cavan, E. L., Basedow, S. L., Briggs, N., Burd, A. B., Darroch, L. J., et al. (2020). Sinking organic particles in the ocean- flux estimates from in situ optical devices. *Frontiers in Marine Science*, *6*(834). doi:10.3389/fmars.2019.00834

Giering, S. L. C., Sanders, R., Martin, A. P., Lindemann, C., Möller, K. O., Daniels, C. J., et al. (2016). High export via small particles before the onset of the North Atlantic spring bloom. *Journal of Geophysical Research: Oceans*, *121*(9), 6929-6945. doi:10.1002/2016jc012048

Green, R. E., Sosik, H. M., & Olson, R. J. (2003a). Contributions of phytoplankton and other particles to inherent optical properties in New England continental shelf waters. *Limnology and Oceanography*, *48*(6), 2377-2391. doi:10.4319/lo.2003.48.6.2377

Green, R. E., Sosik, H. M., Olson, R. J., & DuRand, M. D. (2003b). Flow cytometric determination of size and complex refractive index for marine particles: comparison with independent and bulk estimates. *Applied Optics*, *42*(3), 526-541. doi:10.1364/AO.42.000526

Guidi, L., Chaffron, S., Bittner, L., Eveillard, D., Larhlimi, A., Roux, S., et al. (2016). Plankton networks driving carbon export in the oligotrophic ocean. *Nature*, *532*(7600), 465-470. doi:10.1038/nature16942

Guidi, L., Jackson, G. A., Stemmann, L., Miquel, J. C., Picheral, M., & Gorsky, G. (2008). Relationship between particle size distribution and flux in the mesopelagic zone. *Deep Sea Research Part I: Oceanographic Research Papers*, *55*(10), 1364-1374. doi:10.1016/j.dsr.2008.05.014

Gustafsson, Ö., Andersson, P., Roos, P., Kukulska, Z., Broman, D., Larsson, U., et al. (2004). Evaluation of the collection efficiency of upper ocean sub-photic-layer sediment traps: A 24-month in situ calibration in the open Baltic Sea using 234Th. *Limnology and Oceanography: Methods*, *2*(2), 62-74. doi:10.4319/lom.2004.2.62

Hamm, C. E. (2002). Interactive aggregation and sedimentation of diatoms and clay-sized lithogenic material. *Limnology and Oceanography*, *47*(6), 1790-1795. doi:10.4319/lo.2002.47.6.1790

Hatta, M., Measures, C. I., Wu, J., Roshan, S., Fitzsimmons, J. N., Sedwick, P. N., & Morton, P. L. (2015). An overview of dissolved Fe and Mn distributions during the 2010–2011 US GEOTRACES north Atlantic cruises: GEOTRACES GA03. *Deep Sea Research Part II: Topical Studies in Oceanography*, *116*, 117-129. doi:10.1016/j.dsr2.2014.07.005

Henson, S. A., Sanders, R., & Madsen, E. (2012). Global patterns in efficiency of particulate organic carbon export and transfer to the deep ocean. *Global Biogeochemical Cycles*, *26*(1). doi:10.1029/2011gb004099

Honjo, S., Dymond, J., Collier, R., & Manganini, S. J. (1995). Export production of particles to the interior of the equatorial Pacific Ocean during the 1992 EqPac experiment. *Deep Sea Research Part II: Topical Studies in Oceanography*, *42*(2-3), 831-870. doi:10.1016/0967-0645(95)00034-N

Honjo, S., Krishfield, R. A., Eglinton, T. I., Manganini, S. J., Kemp, J. N., Doherty, K., et al. (2010). Biological pump processes in the cryopelagic and hemipelagic Arctic Ocean: Canada Basin and Chukchi Rise. *Progress in Oceanography*, *85*(3-4), 137-170. doi:10.1016/j.pocean.2010.02.009

Hurd, D. C., & Theyer, F. (1977). Changes in the physical and chemical properties of biogenic silica from the central equatorial Pacific; Part II, Refractive index, density, and water content of acid-cleaned samples. *American Journal of Science*, *277*(9), 1168-1202. doi:10.2475/ajs.277.9.1168

1177 Hwang, J., Kim, M., Manganini, S. J., McIntyre, C. P., Haghipour, N., Park, J., et al. (2015).
1178 Temporal and spatial variability of particle transport in the deep Arctic Canada Basin. *Journal of*
1179 *Geophysical Research: Oceans*, *120*(4), 2784-2799. doi:10.1002/2014jc010643
1180 Iversen, M. H., & Ploug, H. (2010). Ballast minerals and the sinking carbon flux in the ocean:
1181 carbon-specific respiration rates and sinking velocity of marine snow aggregates.
1182 *Biogeosciences*, *7*(9), 2613-2624. doi:10.5194/bg-7-2613-2010
1183 Iversen, M. H., & Robert, M. L. (2015). Ballasting effects of smectite on aggregate formation
1184 and export from a natural plankton community. *Marine Chemistry*, *175*, 18-27.
1185 doi:10.1016/j.marchem.2015.04.009
1186 Jackson, G. A., Maffione, R., Costello, D. K., Alldredge, A. L., Logan, B. E., & Dam, H. G.
1187 (1997). Particle size spectra between 1 μm and 1 cm at Monterey Bay determined using multiple
1188 instruments. *Deep Sea Research Part I: Oceanographic Research Papers*, *44*(11), 1739-1767.
1189 doi:10.1016/S0967-0637(97)00029-0
1190 Jakobsson, M. (2002). Hypsometry and volume of the Arctic Ocean and its constituent seas.
1191 *Geochemistry, Geophysics, Geosystems*, *3*(5), 1-18. doi:10.1029/2001GC000302
1192 Jenkinson, I. R. (1986). Oceanographic implications of non-newtonian properties found in
1193 phytoplankton cultures. *Nature*, *323*(6087), 435-437. doi:10.1038/323435a0
1194 Jenkinson, I. R. (1993). Bulk-phase viscoelastic properties of seawater. *Oceanol. acta*, *16*(4),
1195 317-334.
1196 Jenkinson, I. R., & Biddanda, B. A. (1995). Bulk-phase viscoelastic properties of seawater
1197 relationship with plankton components. *Journal of Plankton Research*, *17*(12), 2251-2274.
1198 doi:10.1093/plankt/17.12.2251
1199 Kindler, K., Khalili, A., & Stocker, R. (2010). Diffusion-limited retention of porous particles
1200 at density interfaces. *Proceedings of the National Academy of Sciences*, *107*(51), 22163-22168.
1201 doi:10.1073/pnas.1012319108
1202 Kiørboe, T., Ploug, H., & Thygesen, U. H. (2001). Fluid motion and solute distribution
1203 around sinking aggregates. I. Small-scale fluxes and heterogeneity of nutrients in the pelagic
1204 environment. *Marine Ecology Progress Series*, *211*, 1-13. doi:10.3354/meps211001
1205 Kipp, L. E., Sanial, V., Henderson, P. B., van Beek, P., Reyss, J. L., Hammond, D. E., et al.
1206 (2018). Radium isotopes as tracers of hydrothermal inputs and neutrally buoyant plume
1207 dynamics in the deep ocean. *Marine Chemistry*, *201*, 51-65. doi:10.1016/j.marchem.2017.06.011
1208 Klaas, C., & Archer, D. E. (2002). Association of sinking organic matter with various types of
1209 mineral ballast in the deep sea: Implications for the rain ratio. *Global Biogeochemical Cycles*,
1210 *16*(4), 63-61-63-14. doi:10.1029/2001GB001765
1211 Krishnaswami, S., Sarin, M. M., & Somayajulu, B. L. K. (1981). Chemical and radiochemical
1212 investigations of surface and deep particles of the Indian Ocean. *Earth and Planetary Science*
1213 *Letters*, *54*(1), 81-96. doi:10.1016/0012-821X(81)90071-6
1214 Kwon, E. Y., Primeau, F., & Sarmiento, J. L. (2009). The impact of remineralization depth on
1215 the air–sea carbon balance. *Nature Geoscience*, *2*(9), 630-635. doi:10.1038/ngeo612
1216 Lam, P. J., & Bishop, J. K. B. (2007). High biomass, low export regimes in the Southern
1217 Ocean. *Deep Sea Research Part II: Topical Studies in Oceanography*, *54*(5-7), 601-638.
1218 doi:10.1016/j.dsr2.2007.01.013
1219 Lam, P. J., Doney, S. C., & Bishop, J. K. B. (2011). The dynamic ocean biological pump:
1220 Insights from a global compilation of particulate organic carbon, CaCO3, and opal concentration
1221 profiles from the mesopelagic. *Global Biogeochemical Cycles*, *25*(3).
1222 doi:10.1029/2010gb003868

Lam, P. J., Lee, J. M., Heller, M. I., Mehic, S., Xiang, Y., & Bates, N. R. (2018). Size-fractionated distributions of suspended particle concentration and major phase composition from the US GEOTRACES Eastern Pacific Zonal Transect (GP16). *Marine Chemistry*, *201*, 90-107. doi:10.1016/j.marchem.2017.08.013

Lam, P. J., & Marchal, O. (2015). Insights into particle cycling from thorium and particle data. *Annual review of marine science*, *7*, 159-184. doi:10.1146/annurev-marine-010814-015623

Lam, P. J., Ohnemus, D. C., & Auro, M. E. (2015). Size-fractionated major particle composition and concentrations from the US GEOTRACES North Atlantic Zonal Transect. *Deep Sea Research Part II: Topical Studies in Oceanography*, *116*, 303-320. doi:10.1016/j.dsr2.2014.11.020

Laufkötter, C., Vogt, M., Gruber, N., Aumont, O., Bopp, L., Doney, S. C., et al. (2016). Projected decreases in future marine export production: the role of the carbon flux through the upper ocean ecosystem. *Biogeosciences*, *13*(13), 4023-4047. doi:10.5194/bg-13-4023-2016

Laurenceau-Cornec, E. C., Le Moigne, F. A. C., Gallinari, M., Moriceau, B., Toullec, J., Iversen, M. H., et al. (2020). New guidelines for the application of Stokes' models to the sinking velocity of marine aggregates. *Limnology and Oceanography*, *65*(6), 1264-1285. doi:10.1002/lno.11388

Laurenceau-Cornec, E. C., Trull, T. W., Davies, D. M., Bray, S. G., Doran, J., Planchon, F., et al. (2015a). The relative importance of phytoplankton aggregates and zooplankton fecal pellets to carbon export: insights from free-drifting sediment trap deployments in naturally iron-fertilised waters near the Kerguelen Plateau. *Biogeosciences*, *12*(4), 1007-1027. doi:10.5194/bg-12-1007-2015

Laurenceau-Cornec, E. C., Trull, T. W., Davies, D. M., Christina, L., & Blain, S. (2015b). Phytoplankton morphology controls on marine snow sinking velocity. *Marine Ecology Progress Series*, *520*, 35-56. doi:10.3354/meps11116

Le Moigne, F. A. C., Sanders, R. J., Villa-Alfageme, M., Martin, A. P., Pabortsava, K., Planquette, H., et al. (2012). On the proportion of ballast versus non-ballast associated carbon export in the surface ocean. *Geophysical research letters*, *39*(15). doi:10.1029/2012GL052980

Lee, C., Peterson, M. L., Wakeham, S. G., Armstrong, R. A., Cochran, J. K., Miquel, J. C., et al. (2009). Particulate organic matter and ballast fluxes measured using time-series and settling velocity sediment traps in the northwestern Mediterranean Sea. *Deep Sea Research Part II: Topical Studies in Oceanography*, *56*(18), 1420-1436. doi:10.1016/j.dsr2.2008.11.029

Lee, J. M., Heller, M. I., & Lam, P. J. (2018). Size distribution of particulate trace elements in the U.S. GEOTRACES Eastern Pacific Zonal Transect (GP16). *Marine Chemistry*, *201*, 108-123. doi:10.1016/j.marchem.2017.09.006

Lerner, P., Marchal, O., Lam, P. J., Buesseler, K., & Charette, M. A. (2017). Kinetics of thorium and particle cycling along the U.S. GEOTRACES North Atlantic Transect. *Deep Sea Research Part I: Oceanographic Research Papers*, *125*, 106-128. doi:10.1016/j.dsr.2017.05.003

Lima, I. D., Lam, P. J., & Doney, S. C. (2014). Dynamics of particulate organic carbon flux in a global ocean model. *Biogeosciences*, *11*(4), 1177-1198. doi:10.5194/bg-11-1177-2014

Logan, B. E., & Alldredge, A. L. (1989). Potential for increased nutrient uptake by flocculating diatoms. *Marine Biology*, *101*(4), 443-450. doi:10.1007/BF00541645

Logan, B. E., & Wilkinson, D. B. (1990). Fractal geometry of marine snow and other biological aggregates. *Limnology and Oceanography*, *35*(1), 130-136. doi:10.4319/lo.1990.35.1.0130

Loisel, H., Nicolas, J. M., Sciandra, A., Stramski, D., & Poteau, A. (2006). Spectral dependency of optical backscattering by marine particles from satellite remote sensing of the global ocean. *Journal of Geophysical Research: Oceans*, *111*(C9). doi:10.1029/2005JC003367

MacIntyre, S., Alldredge, A. L., & Gotschalk, C. C. (1995). Accumulation of marines now at density discontinuities in the water column. *Limnology and Oceanography*, *40*(3), 449-468. doi:10.4319/lo.1995.40.3.0449

Mahowald, N. M., Baker, A. R., Bergametti, G., Brooks, N., Duce, R. A., Jickells, T. D., et al. (2005). Atmospheric global dust cycle and iron inputs to the ocean. *Global Biogeochemical Cycles*, *19*(4), n/a-n/a. doi:10.1029/2004gb002402

Mandernack, K. W., & Tebo, B. M. (1993). Manganese scavenging and oxidation at hydrothermal vents and in vent plumes. *Geochimica et Cosmochimica Acta*, *57*(16), 3907-3923. doi:10.1016/0016-7037(93)90343-U

Marsay, C. M., Kadko, D., Landing, W. M., Morton, P. L., Summers, B. A., & Buck, C. S. (2018). Concentrations, provenance and flux of aerosol trace elements during US GEOTRACES Western Arctic cruise GN01. *Chemical Geology*, *502*, 1-14. doi:10.1016/j.chemgeo.2018.06.007

Martin, J. H., Knauer, G. A., Karl, D. M., & Broenkow, W. W. (1987). VERTEX: carbon cycling in the northeast Pacific. *Deep Sea Research Part A. Oceanographic Research Papers*, *34*(2), 267-285. doi:10.1016/0198-0149(87)90086-0

McDonnell, A. M., & Buesseler, K. O. (2010). Variability in the average sinking velocity of marine particles. *Limnology and Oceanography*, *55*(5), 2085-2096. doi:10.4319/lo.2010.55.5.2085

McDonnell, A. M. P., & Buesseler, K. O. (2012). A new method for the estimation of sinking particle fluxes from measurements of the particle size distribution, average sinking velocity, and carbon content. *Limnology and Oceanography: Methods*, *10*(5), 329-346. doi:10.4319/lom.2012.10.329

Millero, F. J. (1974). Seawater as a multicomponent electrolyte solution. In E. D. Goldberg (Eds.), *The Sea, Volume 5: Marine Chemistry* (pp. 3-80): John Wiley & Sons Inc.

Nowald, N., Fischer, G., Ratmeyer, V., Iversen, M., Reuter, C., & Wefer, G. (2009). *In-situ sinking speed measurements of marine snow aggregates acquired with a settling chamber mounted to the Cherokee ROV*. Paper presented at Oceans 2009-Europe, IEEE.

Nowald, N., Iversen, M. H., Fischer, G., Ratmeyer, V., & Wefer, G. (2015). Time series of in-situ particle properties and sediment trap fluxes in the coastal upwelling filament off Cape Blanc, Mauritania. *Progress in Oceanography*, *137*, 1-11. doi:10.1016/j.pocean.2014.12.015

Omand, M. M., Govindarajan, R., He, J., & Mahadevan, A. (2020). Sinking flux of particulate organic matter in the oceans: Sensitivity to particle characteristics. *Scientific reports*, *10*(1), 1-16. doi:10.1038/s41598-020-60424-5

Passow, U. (2002). Transparent exopolymer particles (TEP) in aquatic environments. *Progress in Oceanography*, *55*(3), 287-333. doi:10.1016/S0079-6611(02)00138-6

Passow, U., & De La Rocha, C. L. (2006). Accumulation of mineral ballast on organic aggregates. *Global Biogeochemical Cycles*, *20*(1). doi:10.1029/2005gb002579

Passow, U., De La Rocha, C. L., Fairfield, C., & Schmidt, K. (2014). Aggregation as a function of and mineral particles. *Limnology and Oceanography*, *59*(2), 532-547. doi:10.4319/lo.2014.59.2.0532

Pavia, F. J., Anderson, R. F., Lam, P. J., Cael, B. B., Vivancos, S. M., Fleisher, M. Q., et al. (2019). Shallow particulate organic carbon regeneration in the South Pacific Ocean. *Proceedings of the National Academy of Sciences*, *116*(20), 9753-9758. doi:10.1073/pnas.1901863116

Peters, B. D., Lam, P. J., & Casciotti, K. L. (2018). Nitrogen and oxygen isotope measurements of nitrate along the US GEOTRACES Eastern Pacific Zonal Transect (GP16) yield insights into nitrate supply, remineralization, and water mass transport. *Marine Chemistry*, *201*, 137-150. doi:10.1016/j.marchem.2017.09.009

Peterson, M. L., Wakeham, S. G., Lee, C., Askea, M. A., & Miquel, J. C. (2005). Novel techniques for collection of sinking particles in the ocean and determining their settling rates. *Limnology and Oceanography: Methods*, *3*(12), 520-532. doi:10.4319/lom.2005.3.520

Picheral, M., Colin, S., & Irisson, J. O. (2017). EcoTaxa, a tool for the taxonomic classification of images. Available from: http://ecotaxa.obs-vlfr.fr

Pilskaln, C. H., Lehmann, C., Paduan, J. B., & Silver, M. W. (1998). Spatial and temporal dynamics in marine aggregate abundance, sinking rate and flux: Monterey Bay, central California. *Deep Sea Research Part II: Topical Studies in Oceanography*, *45*(8-9), 1803-1837. doi:10.1016/S0967-0645(98)80018-0

Ploug, H., Iversen, M. H., & Fischer, G. (2008a). Ballast, sinking velocity, and apparent diffusivity within marine snow and zooplankton fecal pellets: Implications for substrate turnover by attached bacteria. *Limnology and Oceanography*, *53*(5), 1878-1886. doi:10.4319/lo.2008.53.5.1878

Ploug, H., Iversen, M. H., Koski, M., & Buitenhuis, E. T. (2008b). Production, oxygen respiration rates, and sinking velocity of copepod fecal pellets: direct measurements of ballasting by opal and calcite. *Limnology and Oceanography*, *53*(2), 469-476. doi:10.4319/lo.2008.53.2.0469

Ploug, H., & Passow, U. (2007). Direct measurement of diffusivity within diatom aggregates containing transparent exopolymer particles. *Limnology and oceanography*, *52*(1), 1-6. doi:10.4319/lo.2007.52.1.0001

Prairie, J. C., Ziervogel, K., Arnosti, C., Camassa, R., Falcon, C., Khatri, S., et al. (2013). Delayed settling of marine snow at sharp density transitions driven by fluid entrainment and diffusion-limited retention. *Marine Ecology Progress Series*, *487*, 185-200. doi:10.3354/meps10387

Prairie, J. C., Ziervogel, K., Camassa, R., McLaughlin, R. M., White, B. L., Dewald, C., & Arnosti, C. (2015). Delayed settling of marine snow: Effects of density gradient and particle properties and implications for carbon cycling. *Marine Chemistry*, *175*, 28-38. doi:10.1016/j.marchem.2015.04.006

Puigcorbé, V., Benitez-Nelson, C. R., Masqué, P., Verdeny, E., White, A. E., Popp, B. N., et al. (2015). Small phytoplankton drive high summertime carbon and nutrient export in the Gulf of California and Eastern Tropical North Pacific. *Global Biogeochemical Cycles*, *29*(8), 1309-1332. doi:10.1002/2015gb005134

Rea, D. K., & Hovan, S. A. (1995). Grain size distribution and depositional processes of the mineral component of abyssal sediments: Lessons from the North Pacific. *Paleoceanography*, *10*(2), 251-258. doi:10.1029/94PA03355

Resing, J. A., Sedwick, P. N., German, C. R., Jenkins, W. J., Moffett, J. W., Sohst, B. M., & Tagliabue, A. (2015). Basin-scale transport of hydrothermal dissolved metals across the South Pacific Ocean. *Nature*, *523*(7559), 200-203. doi:10.1038/nature14577

Reynolds, R. A., Stramski, D., & Neukermans, G. (2016). Optical backscattering by particles in Arctic seawater and relationships to particle mass concentration, size distribution, and bulk composition. *Limnology and Oceanography*, *61*(5), 1869-1890. doi:10.1002/lno.10341

Riley, J. S., Sanders, R., Marsay, C., Le Moigne, F. A. C., Achterberg, E. P., & Poulton, A. J. (2012). The relative contribution of fast and slow sinking particles to ocean carbon export. *Global Biogeochemical Cycles*, *26*(1), n/a-n/a. doi:10.1029/2011gb004085

Rixen, T., Gaye, B., Emeis, K., & Ramaswamy, V. (2019). The ballast effect of lithogenic matter and its influences on the carbon fluxes in the Indian Ocean. *Biogeosciences*, *16*(2), 485-503. doi:10.5194/bg-16-485-2019

Rohatgi, A. (2010). WebPlotDigitizer- Extract data from plots, images, and maps. Available from: https://automeris.io/WebPlotDigitizer/

Rosengard, S. Z., Lam, P. J., Balch, W. M., Auro, M. E., Pike, S., Drapeau, D., & Bowler, B. (2015). Carbon export and transfer to depth across the Southern Ocean Great Calcite Belt. *Biogeosciences*, *12*(13), 3953-3971. doi:10.5194/bg-12-3953-2015

Roullier, F., Berline, L., Guidi, L., Durrieu De Madron, X., Picheral, M., Sciandra, A., et al. (2014). Particle size distribution and estimated carbon flux across the Arabian Sea oxygen minimum zone. *Biogeosciences*, *11*(16), 4541-4557. doi:10.5194/bg-11-4541-2014

Ruiz, J. (1997). What generates daily cycles of marine snow? *Deep Sea Research Part I: Oceanographic Research Papers*, *44*(7), 1105-1126. doi:10.1016/S0967-0637(97)00012-5

Rutgers van der Loeff, M. M., & Berger, G. W. (1993). Scavenging of 230Th and 231Pa near the antarctic polar front in the South Atlantic. *Deep Sea Research Part I: Oceanographic Research Papers*, *40*(2), 339-357. doi:10.1016/0967-0637(93)90007-P

Santschi, P. H., Murray, J. W., Baskaran, M., Benitez-Nelson, C. R., Guo, L. D., Hung, C. C., et al. (2006). Thorium speciation in seawater. *Marine Chemistry*, *100*(3), 250-268. doi:10.1016/j.marchem.2005.10.024

Schlitzer, R., Anderson, R. F., Dodas, E. M., Lohan, M., Geibert, W., Tagliabue, A., et al. (2018). The GEOTRACES intermediate data product 2017. *Chemical Geology*, *493*(C), 210-223. doi:10.1016/j.chemgeo.2018.05.040

Schmidt, K., De La Rocha, C. L., Gallinari, M., & Cortese, G. (2014). Not all calcite ballast is created equal: differing effects of foraminiferan and coccolith calcite on the formation and sinking of aggregates. *Biogeosciences*, *11*(1), 135-145. doi:10.5194/bg-11-135-2014

Scholten, J. C., Rutgers van der Loeff, M. M., & Michel, A. (1995). Distribution of 230Th and 231Pa in the water column in relation to the ventilation of the deep Arctic basins. *Deep Sea Research Part II: Topical Studies in Oceanography*, *42*(6), 1519-1531. doi:10.1016/0967-0645(95)00052-6

Seuront, L., Lacheze, C., Doubell, M. J., Seymour, J. R., Van Dongen-Vogels, V., Newton, K., et al. (2007). The influence of Phaeocystis globosa on microscale spatial patterns of chlorophyll a and bulk-phase seawater viscosity. In M. A. van Leeuwe, J. Stefels, S. Belviso, C. Lancelot, P. G. Verity and W. W. C. Gieskes (Eds.), *Phaeocystis, major link in the biogeochemical cycling of climate-relevant elements* (pp. 173-188). Dordrecht: Springer Netherlands. doi:10.1007/978-1-4020-6214-8_13

Seuront, L., Leterme, S. C., Seymour, J. R., Mitchell, J. G., Ashcroft, D., Noble, W., et al. (2010). Role of microbial and phytoplanktonic communities in the control of seawater viscosity off East Antarctica (30-80° E). *Deep Sea Research Part II: Topical Studies in Oceanography*, *57*(9), 877-886. doi:10.1016/j.dsr2.2008.09.018

Seuront, L., & Vincent, D. (2008). Increased seawater viscosity, Phaeocystis globosa spring bloom and Temora longicornis feeding and swimming behaviours. *Marine Ecology Progress Series*, *363*, 131-145. doi:10.3354/meps07373

Seuront, L., Vincent, D., & Mitchell, J. G. (2006). Biologically induced modification of seawater viscosity in the Eastern English Channel during a Phaeocystis globosa spring bloom. *Journal of Marine Systems*, *61*(3), 118-133. doi:10.1016/j.jmarsys.2005.04.010

Shanks, A. L., & Trent, J. D. (1980). Marine snow: sinking rates and potential role in vertical flux. *Deep Sea Research Part A. Oceanographic Research Papers*, *27*(2), 137-143. doi:10.1016/0198-0149(80)90092-8

Smyth, T. J., Tarran, G. A., & Sathyendranath, S. (2019). Marine picoplankton size distribution and optical property contrasts throughout the Atlantic Ocean revealed using flow cytometry. *Applied Optics*, *58*(32), 8802-8815. doi:10.1364/AO.58.008802

Stemmann, L., & Boss, E. (2012). Plankton and particle size and packaging: from determining optical properties to driving the biological pump. *Annual Review of Marine Science*, *4*, 263-290. doi:10.1146/annurev-marine-120710-100853

Stemmann, L., Eloire, D., Sciandra, A., Jackson, G. A., Guidi, L., Picheral, M., & Gorsky, G. (2008). Volume distribution for particles between 3.5 to 2000 μm in the upper 200 m region of the South Pacific Gyre. *Biogeosciences*, *5*(2), 299-310. doi:10.5194/bg-5-299-2008

Stemmann, L., Jackson, G. A., & Ianson, D. (2004). A vertical model of particle size distributions and fluxes in the midwater column that includes biological and physical processes—Part I: model formulation. *Deep Sea Research Part I: Oceanographic Research Papers*, *51*(7), 865-884. doi:10.1016/j.dsr.2004.03.001

Stokes, G. G. (1851). On the effect of the internal friction of fluids on the motion of pendulums. *Transactions of the Cambridge Philosophical Society*, *9*, 8-106.

Stramski, D., Bricaud, A., & Morel, A. (2001). Modeling the inherent optical properties of the ocean based on the detailed composition of the planktonic community. *Applied Optics*, *40*(18), 2929-2945. doi:10.1364/AO.40.002929

Thyng, K. M., Greene, C. A., Hetland, R. D., Zimmerle, H. M., & DiMarco, S. F. (2016). True colors of oceanography: Guidelines for effective and accurate colormap selection. *Oceanography*, *29*(3), 9-13. doi:10.5670/oceanog.2016.66

Torres-Valdés, S., Painter, S. C., Martin, A. P., Sanders, R., & Felden, J. (2014). Data compilation of fluxes of sedimenting material from sediment traps in the Atlantic Ocean. *Earth System Science Data*, *6*(1), 123-145. doi:10.5194/essd-6-123-2014

Towe, K. M., & Bradley, W. F. (1967). Mineralogical constitution of colloidal “hydrous ferric oxides”. *Journal of Colloid and Interface Science*, *24*(3), 384-392. doi:10.1016/0021-9797(67)90266-4

Trull, T. W., Bray, S. G., Buesseler, K. O., Lamborg, C. H., Manganini, S., Moy, C., & Valdes, J. (2008). In situ measurement of mesopelagic particle sinking rates and the control of carbon transfer to the ocean interior during the Vertical Flux in the Global Ocean (VERTIGO) voyages in the North Pacific. *Deep Sea Research Part II: Topical Studies in Oceanography*, *55*(14), 1684-1695. doi:10.1016/j.dsr2.2008.04.021

Turner, J. T. (2002). Zooplankton fecal pellets, marine snow and sinking phytoplankton blooms. *Aquatic microbial ecology*, *27*(1), 57-102. doi:10.3354/ame027057

Turner, J. T. (2015). Zooplankton fecal pellets, marine snow, phytodetritus and the ocean’s biological pump. *Progress in Oceanography*, *130*, 205-248. doi:10.1016/j.pocean.2014.08.005

Volk, T., & Hoffert, M. I. (1985). Ocean carbon pumps: analysis of relative strengths and efficiencies in ocean-driven atmospheric CO2 changes. In E. T. Sundquist and W. S. Broecker (Eds.), *The carbon cycle and atmospheric CO2: natural variations Archean to present* (Vol. 32, pp. 99-110). Washington, D. C.: American Geophysical Union. doi:10.1029/GM032p0099

Wang, W. L., Lee, C., & Primeau, F. W. (2019). A Bayesian statistical approach to inferring particle dynamics from in-situ pump POC and chloropigment data from the Mediterranean Sea. *Marine Chemistry*, *214*, 103654. doi:10.1016/j.marchem.2019.04.006

White, F. M. (1974). *Viscous fluid flow*. New York: McGraw-Hill Inc.

Wilson, S. E., Ruhl, H. A., & Smith, J., K. L. (2013). Zooplankton fecal pellet flux in the abyssal northeast Pacific: A 15 year time-series study. *Limnology and oceanography*, *58*(3), 881-892. doi:10.4319/lo.2013.58.3.0881

Woźniak, S. B., Stramski, D., Stramska, M., Reynolds, R. A., Wright, V. M., Miksic, E. Y., et al. (2010). Optical variability of seawater in relation to particle concentration, composition, and size distribution in the nearshore marine environment at Imperial Beach, California. *Journal of Geophysical Research: Oceans*, *115*(C8). doi:10.1029/2009jc005554

Xiang, Y., & Lam, P. J. (2020). Size-fractionated compositions of marine suspended particles in the Western Arctic Ocean: lateral and vertical sources. *Journal of Geophysical Research: Oceans*, *125*(8), e2020JC016144. doi:10.1029/2020JC016144

Xue, J., & Armstrong, R. A. (2009). An improved "benchmark" method for estimating particle settling velocities from time-series sediment trap fluxes. *Deep Sea Research Part II: Topical Studies in Oceanography*, *56*(18), 1479-1486. doi:10.1016/j.dsr2.2008.11.033

Young, J. R. (1994). Functions of coccoliths. In A. Winter and W. G. Siesser (Eds.), *Coccolithophores* (pp. 63-82). Cambridge, UK: Cambridge University Press.

[Global Biogeochemical Cycles]

Supporting information for

Controls on sinking velocities and mass fluxes of size-fractionated marine particles in recent U.S. GEOTRACES cruises

Yang Xiang[1,*], Phoebe J. Lam[1], Adrian Burd[2]

[1]Department of Ocean Sciences, University of California, Santa Cruz, CA 95064 USA
[2]Department of Marine Sciences, University of Georgia, Athens, GA 30602 USA

*Corresponding author: Yang Xiang, E: yaxiang@ucsc.edu, P: 1-831-212-5119
University of California Santa Cruz, 1156 High Street, Santa Cruz, CA 95064

Contents of this file:

Figures S1-S9
Table S1-S2

Additional supporting information:

Table S3. Size-fractionated mass flux and WSV in three cruises (uploaded separately)

Introduction

The supporting information mostly consists of two types of figures: depth profiles and section plots. Depth profiles are used to describe the difference in particle composition between different cruises. Parameters plotted in section plots include the mass-size spectra power q, derived parameters (WSV and mass flux) in the LSF and SSF, and sensitivity studies on the TOT mass flux. Supplemental tables contain information about sources and details of compiled datasets in the porosity-size relationship, size ranges used in the model, and derived mass flux and WSV in all three cruises.

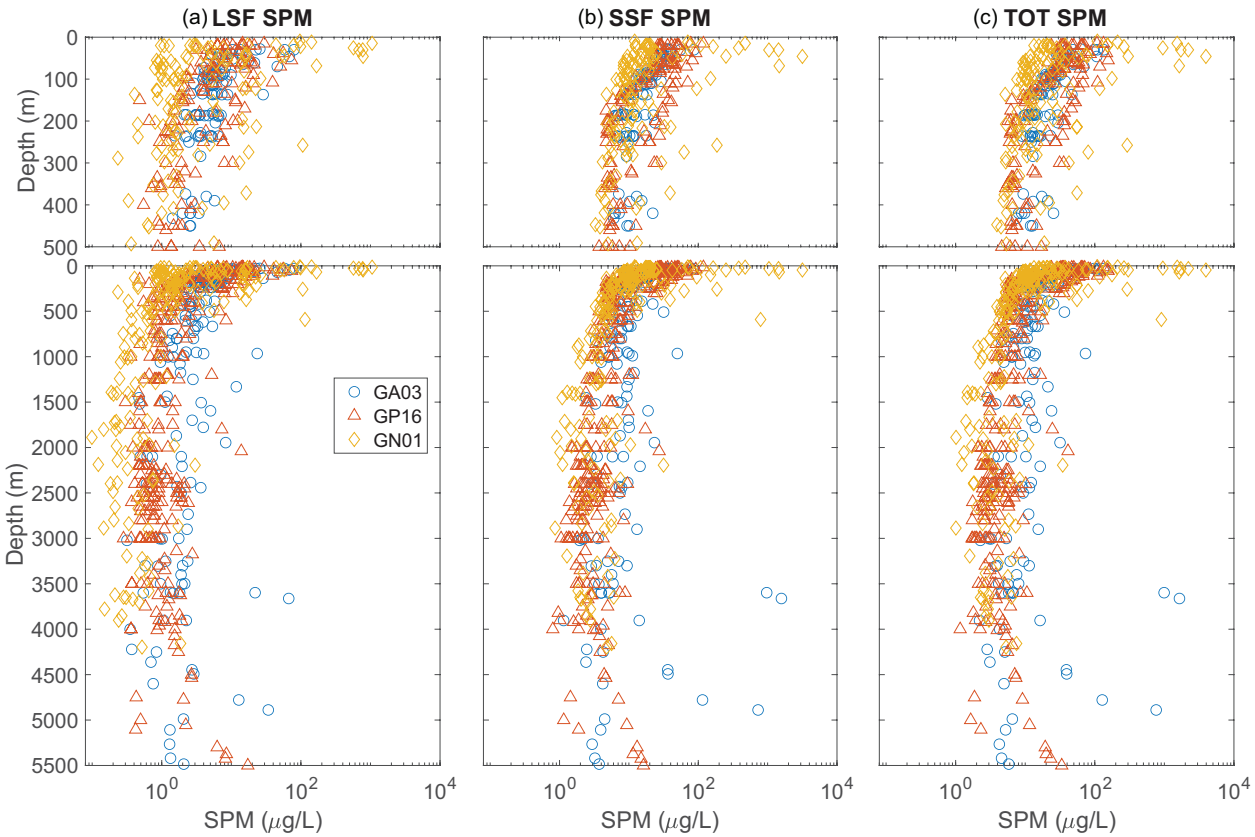

Figure S1. Depth profiles of size-fractionated SPM concentrations (unit: μg/L) in the upper 500 m (top panels) and the whole water column (bottom panels) in all three basins. (a): LSF (>51 μm); (b): SSF (1-51 μm); (c): TOT (>1 μm).

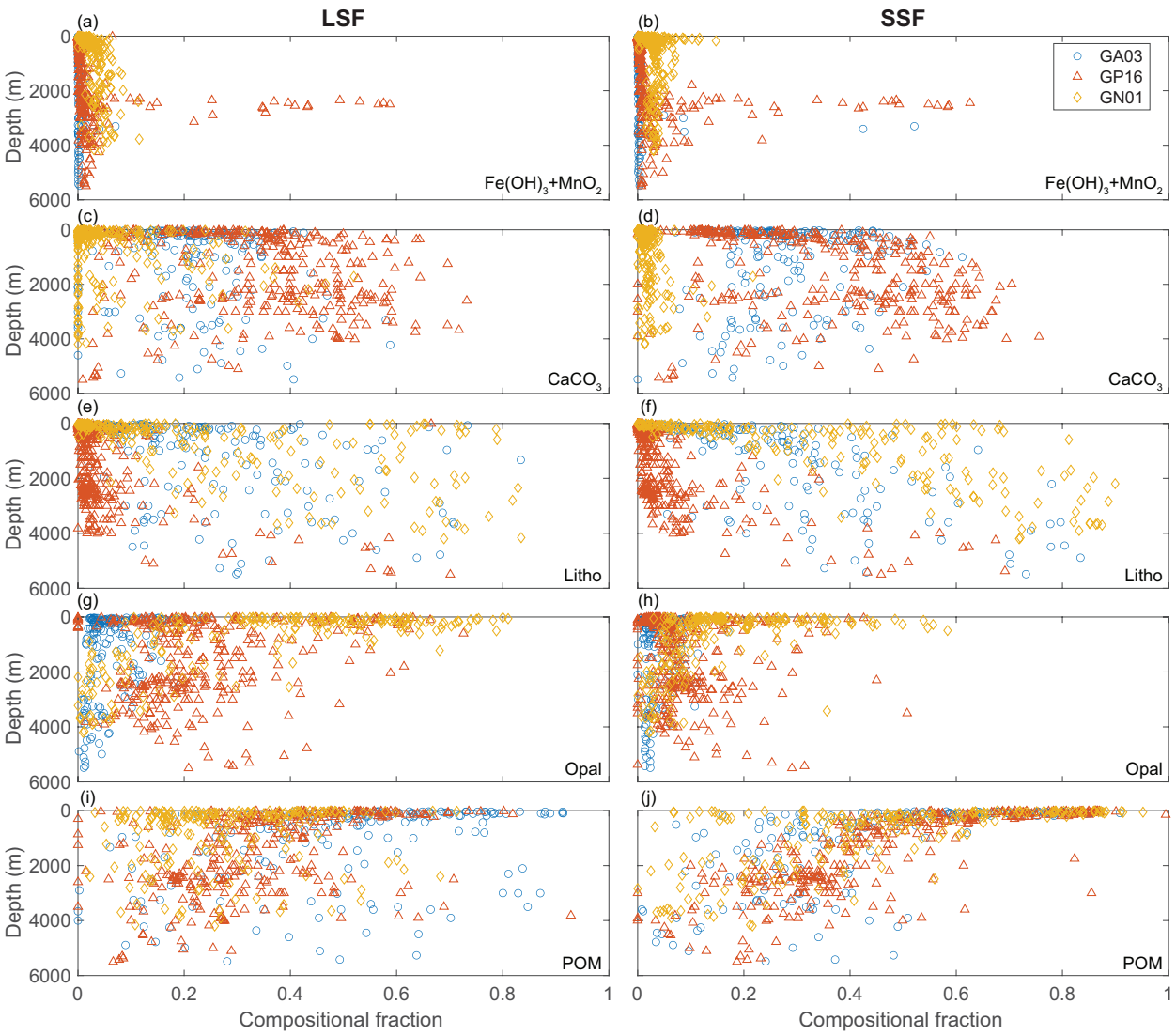

Figure S2. Depth profiles of size-fractionated compositional fractions in the LSF (left panels) and SSF (right panels) in all three basins. (a)-(b): the sum of fractions of iron and manganese (oxyhydr)oxides ($Fe(OH)_3$+MnO_2); (c)-(d): the fractions of calcium carbonate ($CaCO_3$); (e)-(f): the fractions of lithogenic materials (Litho); (g)-(h): the fraction of opal; (i)-(j): the fraction of particulate organic matter (POM).

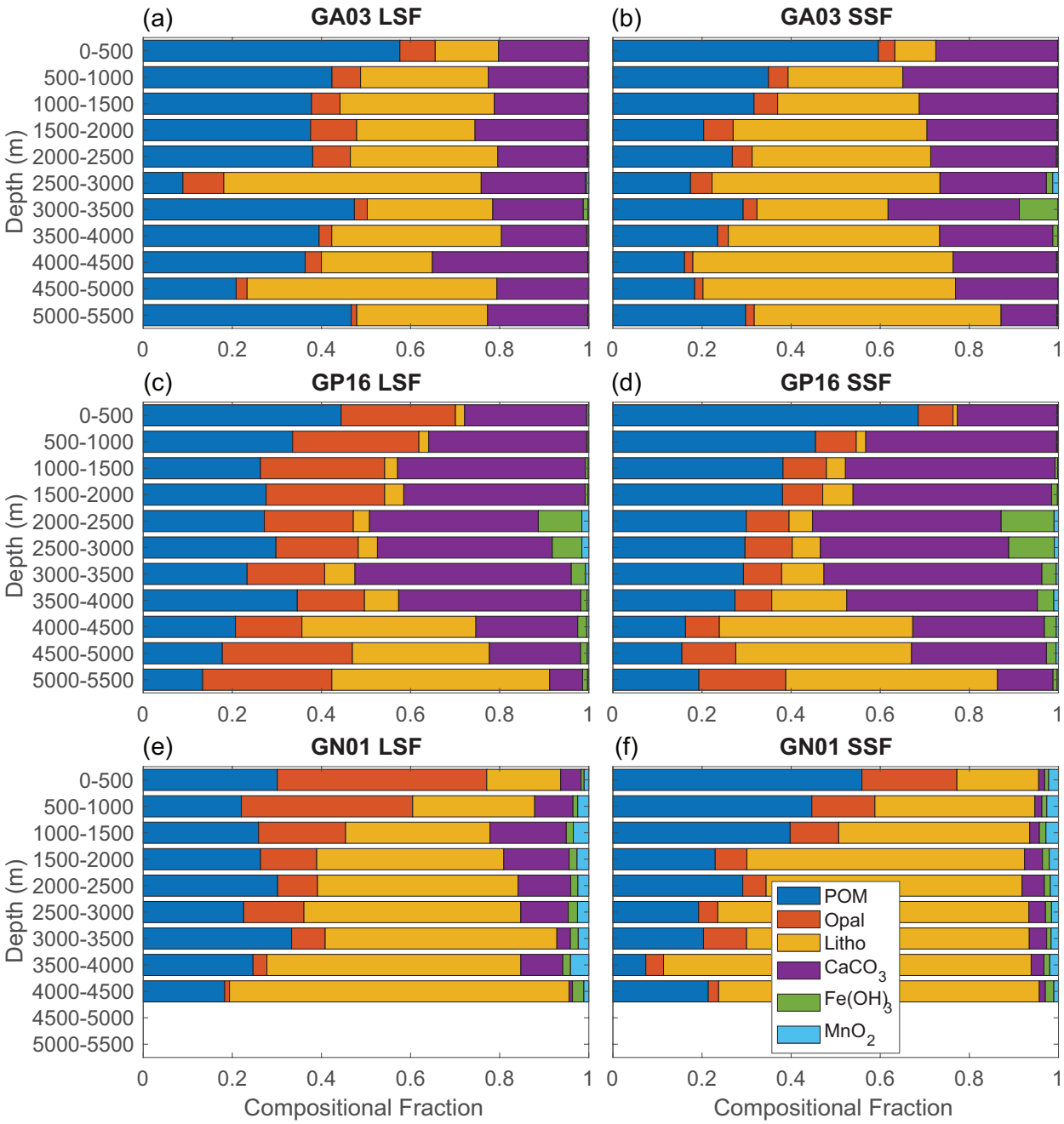

Figure S3. Stacked bar graphs of the change in size-fractionated compositional fractions in all cruises with depth. The left panels are the LSF and right panels are the SSF. Each 500 m depth bin shows the mean compositional fraction over the entire cruise. The blue is the compositional fraction of POM, orange is the fraction of opal, yellow is the fraction of lithogenic, purple is $CaCO_3$, green is Fe oxyhydroxides and light blue is Mn oxides. (a)-(b): GA03; (c)-(d): GP16; (e)-(f): GN01.

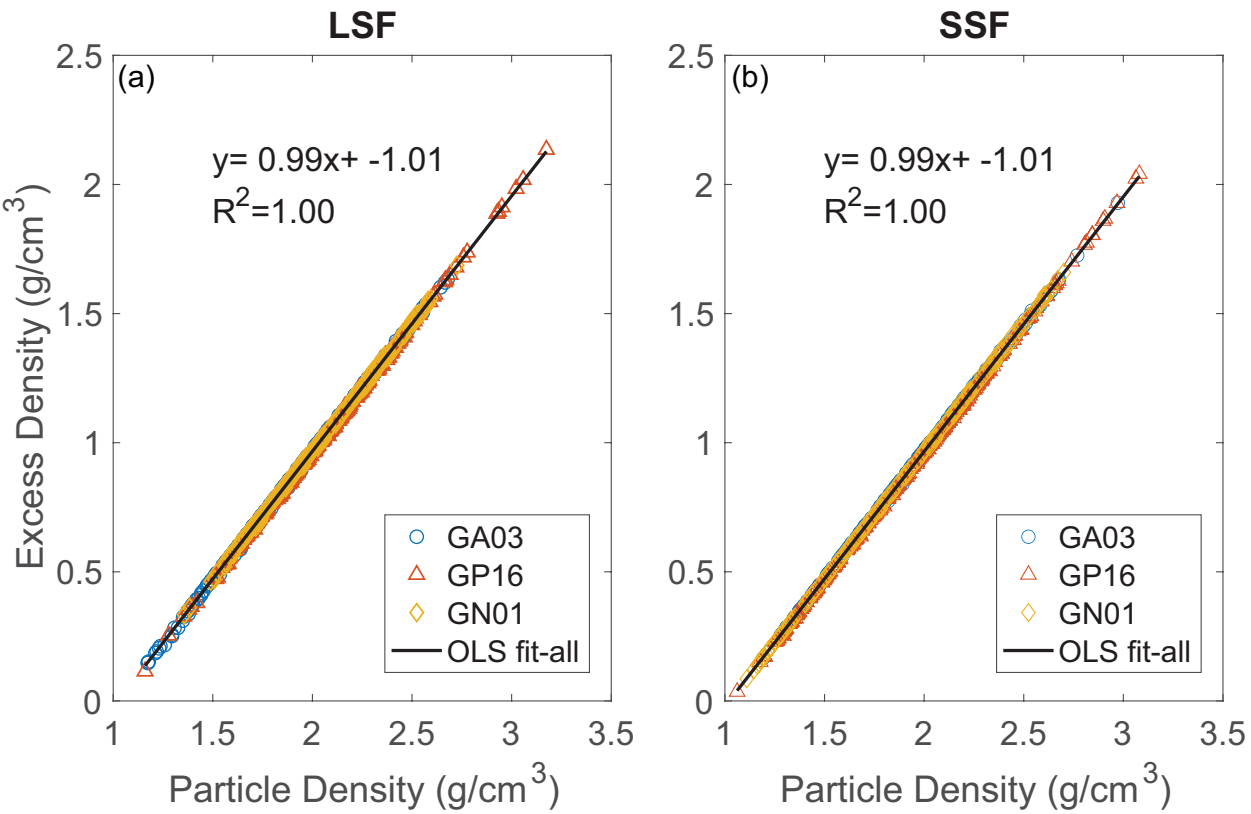

Figure S4. Size-fractionated particle density (unit: g/cm^3) vs. excess density (unit: g/cm^3) in three cruises. (a): LSF; (b): SSF. The ordinary least square (OLS) fit is used in the regression. Regression equations are displayed in each panel.

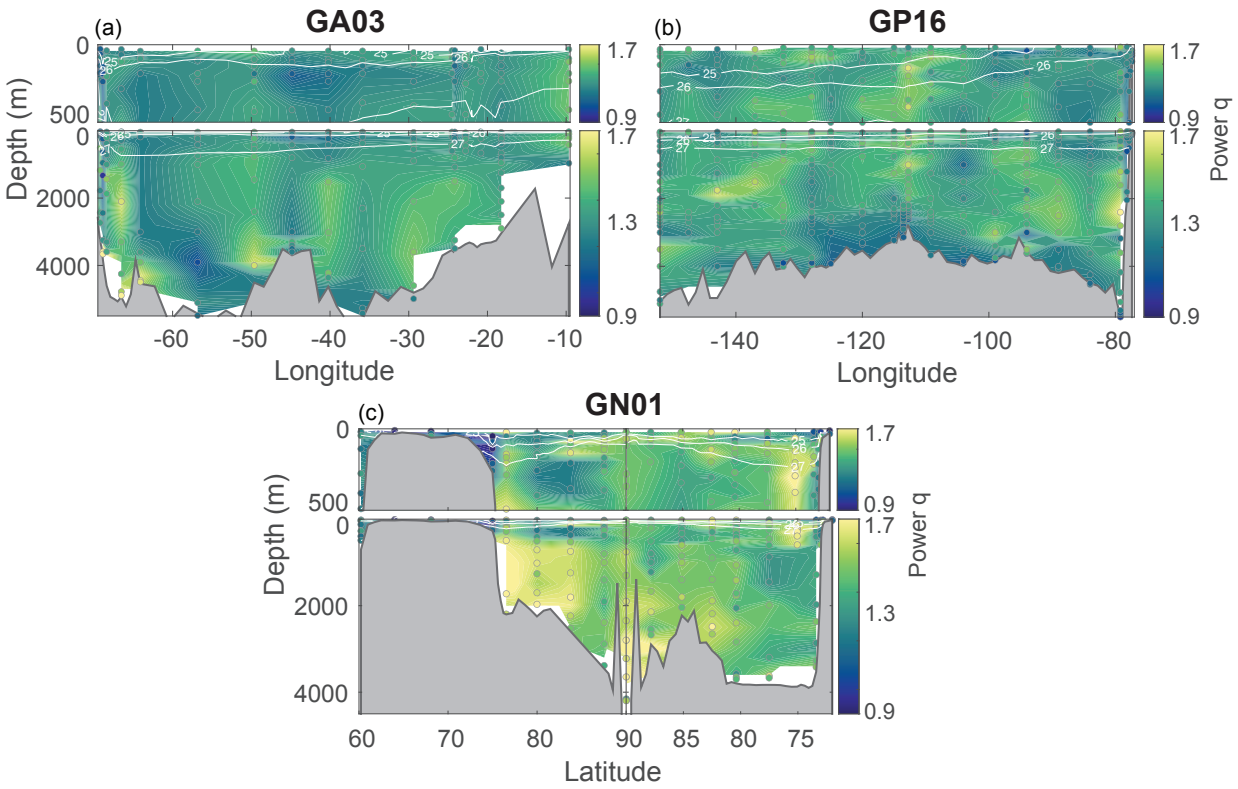

Figure S5. The power exponent q of the mass-size spectra in three cruises. (a): GA03; (b): GP16; (c): GN01. The top panels in each subplot show the upper 500 m, and the lower panels show the entire water column. Thick white contours are potential density anomaly of 25, 26 and 27 kg/m^3.

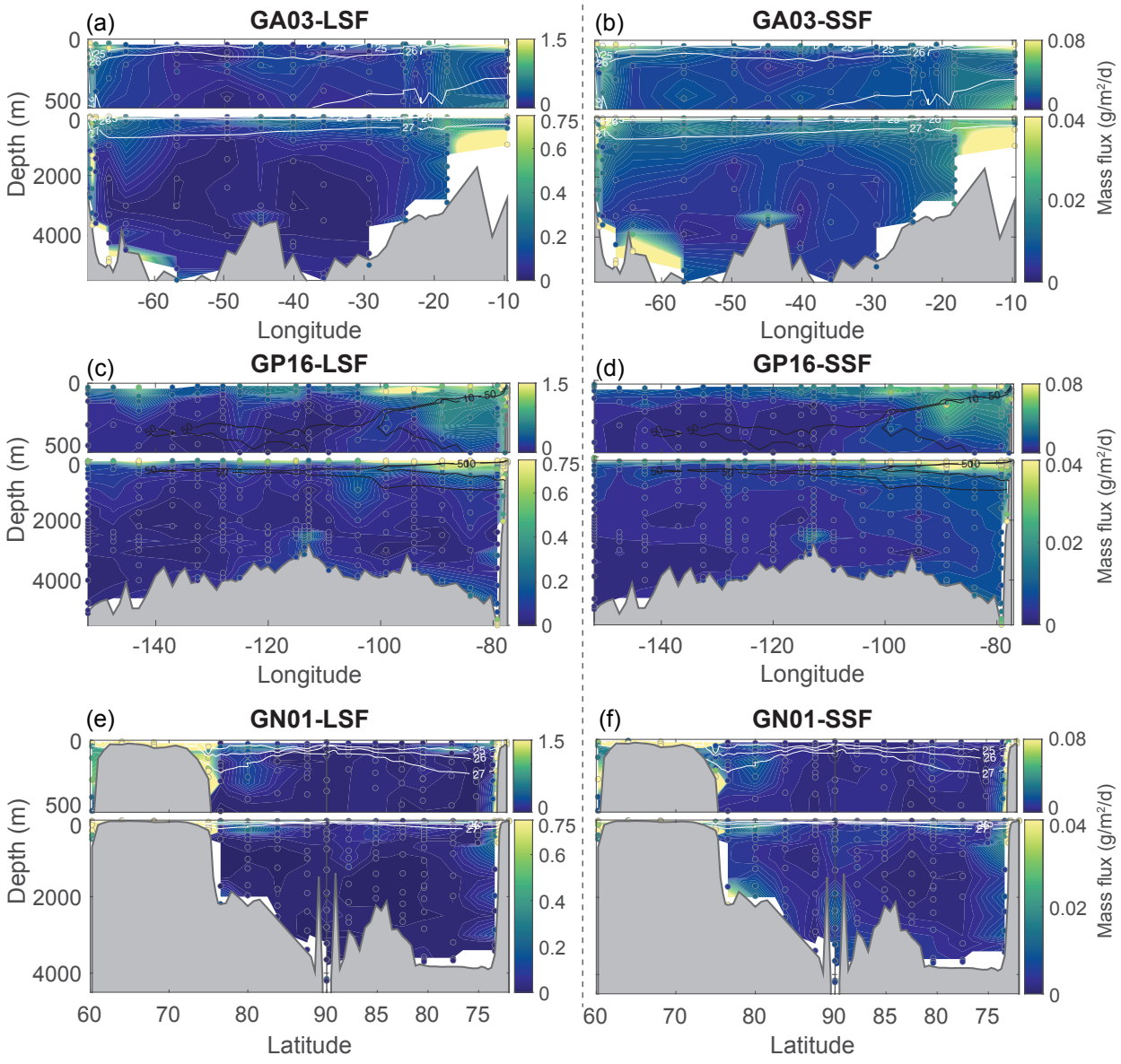

Figure S6. Derived mass flux (unit: g/m^2/d) in the LSF (left panels) and SSF (right panels) in three cruises. (a): GA03 LSF; (b): GA03 SSF; (c): GP16 LSF; (d): GP16 SSF; (e): GN01 LSF; (f): GN01 SSF. Thick white contours are potential density anomaly of 25, 26 and 27 kg/m^3, and thick black contours in the GP16 are dissolved oxygen concentrations of 10 and 50 μmol/kg. Note that color scales are the same for each size fractions in all cruises but are different between the LSF and SSF, and between the upper 500 m and the entire water column.

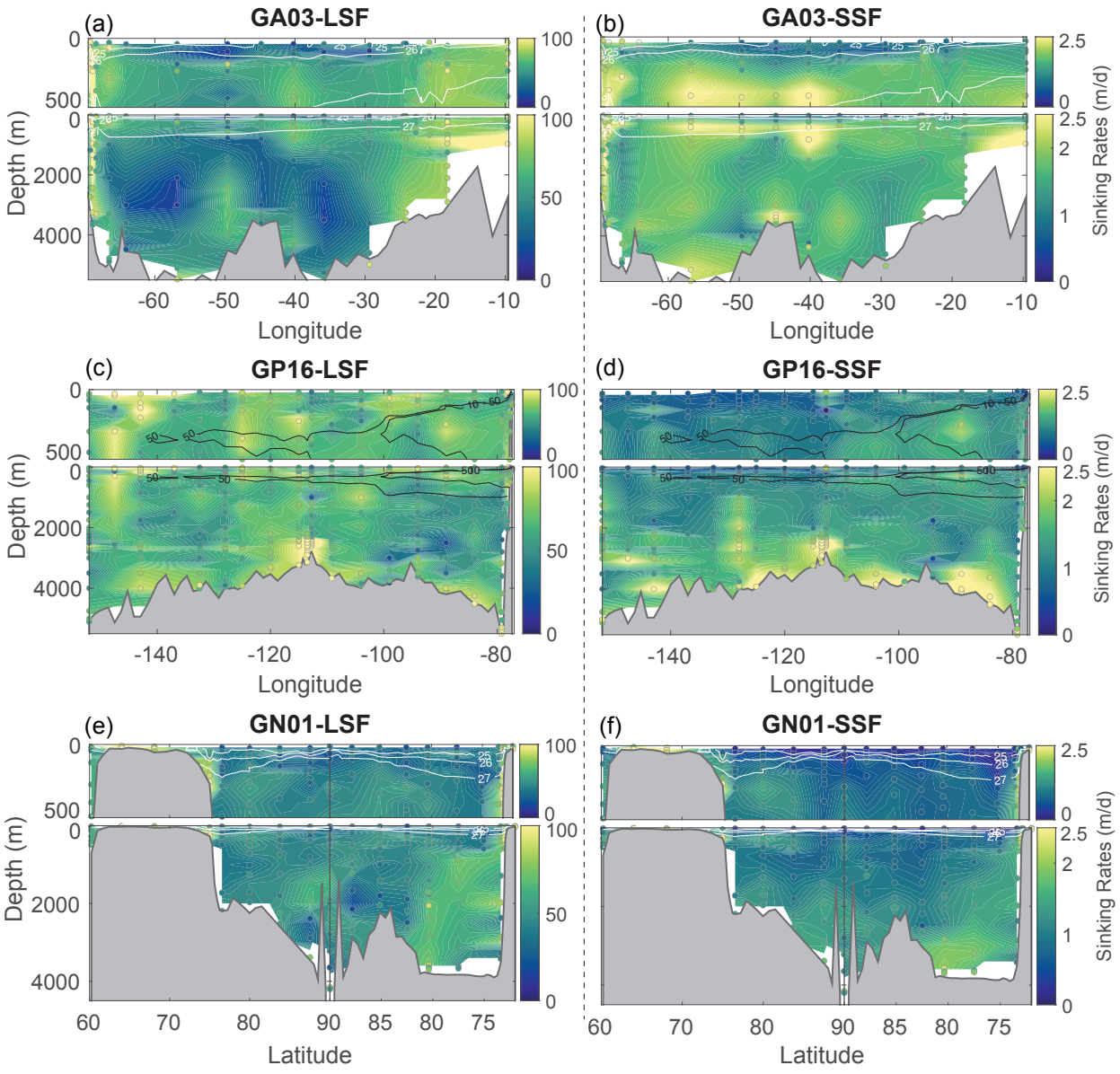

Figure S7. Derived mass-weighted average sinking velocity (unit: m/d) in the LSF (left panels) and SSF (right panels) in three cruises. (a): GA03 LSF; (b): GA03 SSF; (c): GP16 LSF; (d): GP16 SSF; (e) GN01 LSF; (f): GN01 SSF. Contours as for Figure S6.

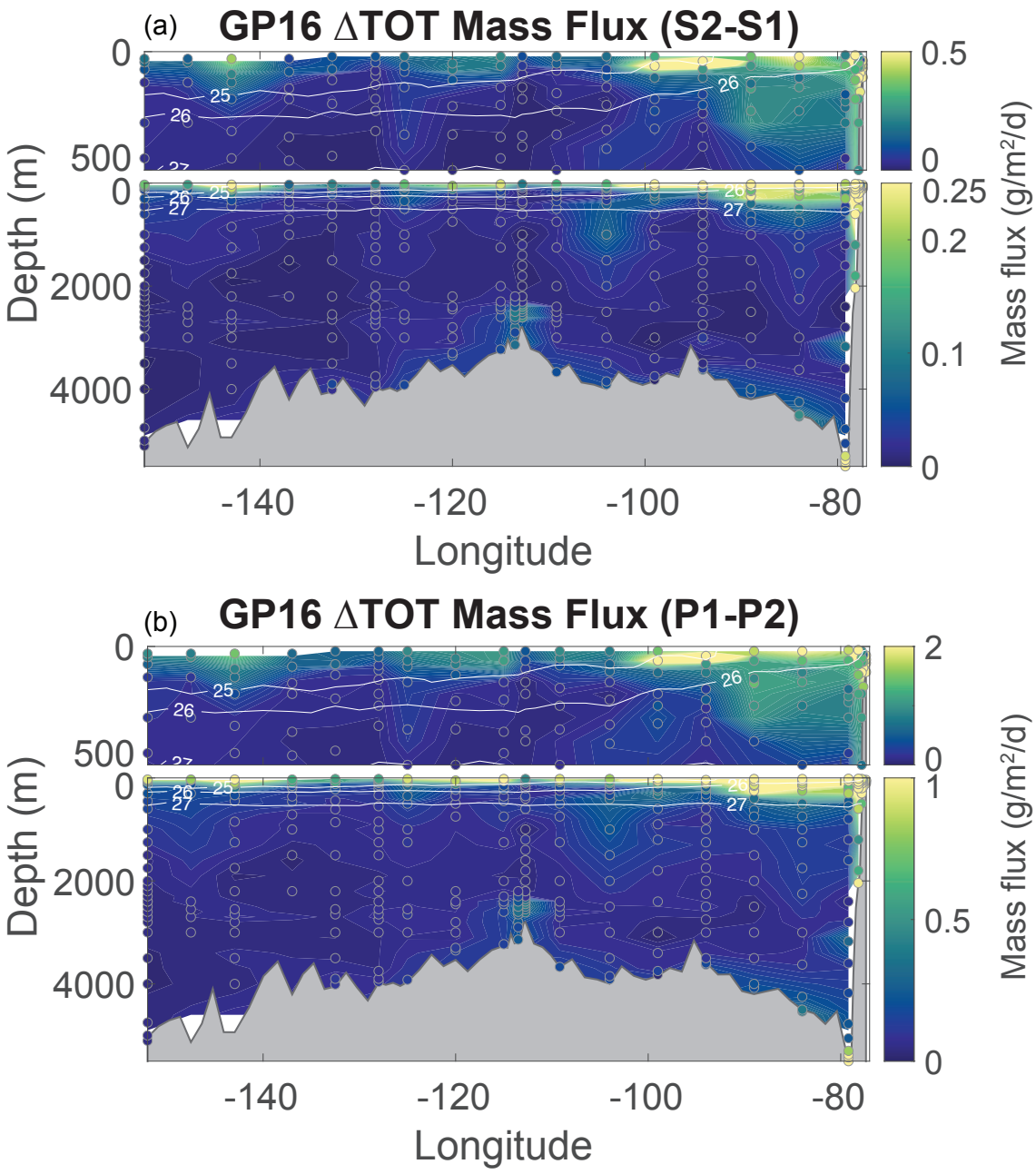

Figure S8. Sensitivity studies. (a) the absolute differences in TOT mass flux between two upper size limits in the LSF (S2-S1), S2 as 10 mm and S1 as 5 mm; (b) the absolute differences in TOT mass flux between two porosity-size relationships (P1-P2), where P1 is the relationship from Alldredge & Gotschalk (1988) and P2 is the newly compiled one in this study. Note that (a) and (b), together with their upper (upper 500 m) and lower (the whole water column) panels, all have different color bars.

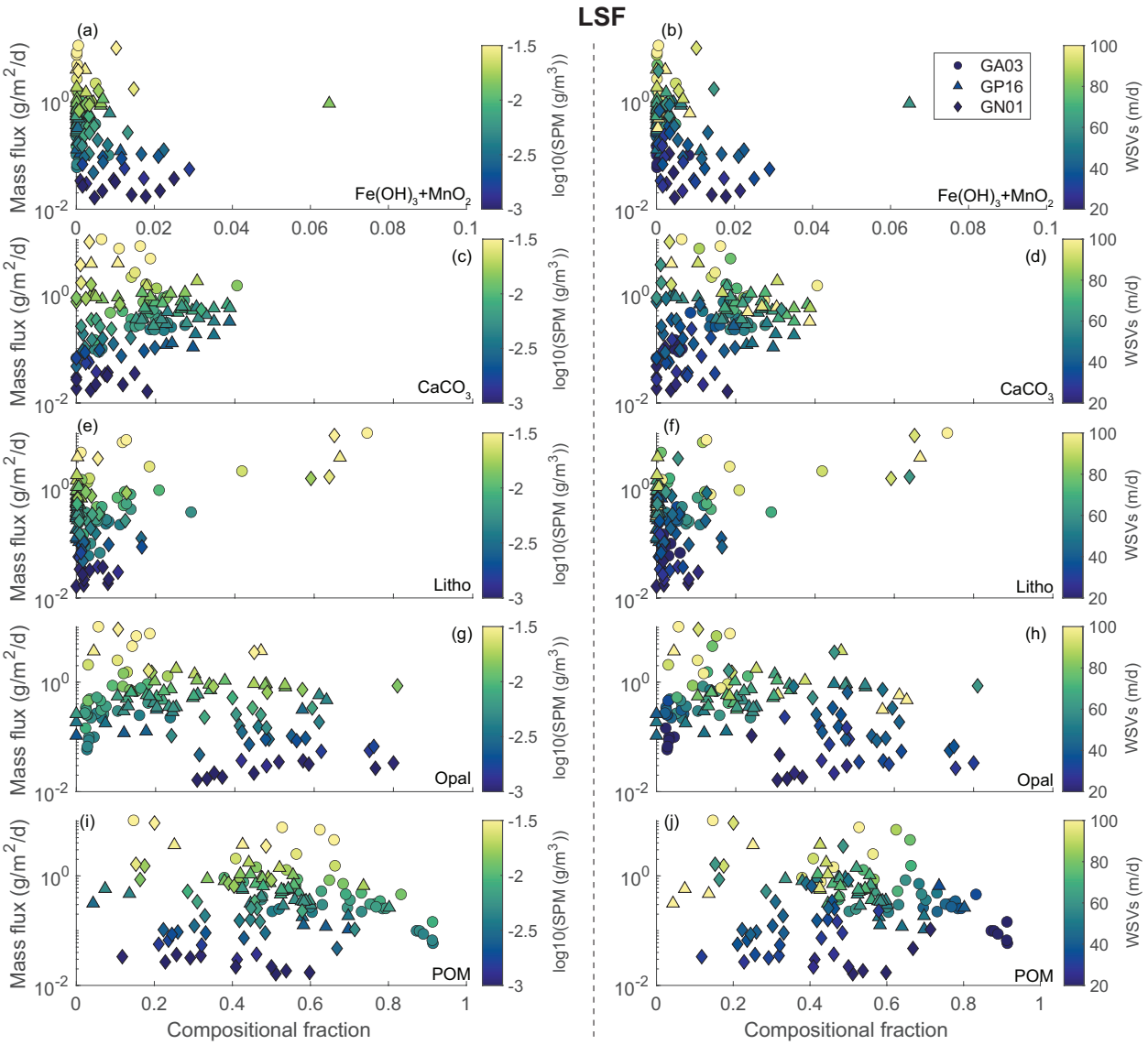

Figure S9. Scatter plots between LSF compositional fractions and LSF mass flux in the upper 100 m of all non-shelf stations (bottom depth>200 m). The color bars are log10(SPM) on the left, and mass-weighted average sinking velocity (WSVs) on the right. Note that the color bar for SPM is in log scale. The first row of plots (a-b) are the compositional fractions of $Fe(OH)_3$+MnO_2, the second row (c-d) the fractions of $CaCO_3$, the third row (e-f) the fractions of Litho, the fourth row (g-h) the fractions of Opal, and the fifth row (i-j) the fraction of POM. The fractions of $Fe(OH)_3$+MnO_2 have different X scales (0-0.1) than other compositional fractions (0-1).

Table S1. *Porosity-size Relationship Literature Compilation*

Sources	Size (Y/N)	Size error (Y/N)	Porosity (Y/N)	Porosity error (Y/N)	Particle Types	How	Size methods	Porosity methods	Data extraction method
Alldredge & Gotschalk, 1988[1]	Y	N	Y	N	Natural diatom & other marine snow	In situ SCUBA divers	Camera-based	Mass-based	Indirectly from Figure 2C
Logan & Alldredge, 1989[2]	Y	N	Y	Y	Natural diatom flocs	In situ SCUBA divers	Camera-based	Mass-based	Directly from Table 2
Lam & Bishop, 2007[3]	Y	Y	Y	N	Natural marine aggregates	In situ pump particles	UVP-based	Mass-based	Indirectly from Figure 14A & UVP PSD slopes
Ploug et al., 2008[4]	Y	Y	Y	Y	Various cultures, marine snow & fecal pellets	Lab roller tanks	Microscope-based	Mass-based	Directly from Table 1
Bach et al., 2016[5]	Y	Y	Y	N	Natural marine aggregates	In situ mesocosm	Camera-based	Mass-based	Personal communication
Ploug & Passow, 2007[6]	Y	Y	Y	Y	Diatom culture	Lab roller tanks	Microscope-based	Mass-based	Directly from Table 1
Engel et al., 2009[7]	Y	Y	Y	Y	*E. huxleyi* cultures	Lab roller tanks	Camera-based	Mass-based	Personal communication
Schmidt et al., 2014[8]	Y	Y	Y	Y	Diatom culture, coccoliths & foram tests	Lab roller tanks	Camera-based	Mass-based	Directly from text & indirectly from Figure 1B
Prairie et al., 2015[9]	Y	Y	Y	Y	Diatom cultures	Lab roller tanks	Microscope-based	Mass-based	Directly from Table 1 & 2
Iversen & Roberts, 2015[10]	Y	N	Y	N	<100 μm natural plankton	Lab roller tanks	Microscope-based	Mass-based	Personal communication
Laurenceau-Cornec et al., 2015[11]	Y	N	Y	N	Natural phytoplankton mixtures	Lab roller tanks	Camera-based	Mass-based	Personal communication
Laurenceau-Cornec et al., 2020[12]	Y	Y	Y	Y	Diatom cultures & zooplankton	Lab roller tanks	Microscope-based	Mass-based	Directly from Tables 2 & S1
Bach et al., 2019[13*]	Y	Y	Y	Y	Natural marine aggregates	In situ mesocosm	Camera-based	Optic-based	Directly from PANGAEA

*. The data from Bach et al. (2019) are not shown in Figure 2 in the main text, for it is optic-based and not calibrated with the mass-based method.

Table S2. *Properties of Size Bins in the Model*

Size bin	SSF			LSF		
	Size min (μm)	Size max (μm)	Center (μm)	Size min (μm)	Size max (μm)	Center (μm)
1	1.0	1.2	1.1	51.0	61.3	55.9
2	1.2	1.4	1.3	61.3	73.6	67.2
3	1.4	1.6	1.5	73.6	88.4	80.7
4	1.6	1.9	1.7	88.4	106.2	96.9
5	1.9	2.2	2.0	106.2	127.6	116.4
6	2.2	2.6	2.4	127.6	153.3	139.9
7	2.6	3.0	2.8	153.3	184.1	168.0
8	3.0	3.5	3.3	184.1	221.2	201.8
9	3.5	4.1	3.8	221.2	265.8	242.5
10	4.1	4.8	4.5	265.8	319.2	291.3
11	4.8	5.6	5.2	319.2	383.5	349.9
12	5.6	6.6	6.1	383.5	460.7	420.4
13	6.6	7.7	7.1	460.7	553.5	505.0
14	7.7	9.0	8.4	553.5	664.9	606.6
15	9.0	10.6	9.8	664.9	798.7	728.8
16	10.6	12.4	11.4	798.7	959.5	875.5
17	12.4	14.5	13.4	959.5	1152.7	1051.7
18	14.5	17.0	15.7	1152.7	1384.8	1263.4
19	17.0	19.8	18.3	1384.8	1663.5	1517.8
20	19.8	23.2	21.5	1663.5	1998.4	1823.3
21	23.2	27.2	25.1	1998.4	2400.7	2190.4
22	27.2	31.8	29.4	2400.7	2884.0	2631.3
23	31.8	37.2	34.4	2884.0	3464.6	3161.0
24	37.2	43.6	40.3	3464.6	4162.1	3797.4
25	43.6	51.0	47.1	4162.1	5000.0	4561.9